Check for updates

ADVANCING EARTH AND SPACE SCIENCES

JAMES Journal of Advances in Modeling Earth Systems®

RESEARCH ARTICLE
10.1029/2025MS004950

Examining the Fidelity of Leith Subgrid Closures for Parameterizing Mesoscale Eddies in Idealized and Global (NEMO) Ocean Models

T. Wilder[1] and **T. Kuhlbrodt**[1]

[1]Department of Meteorology, National Centre for Atmospheric Science, University of Reading, Reading, UK

Abstract Eddy-permitting models struggle to simulate accurate Southern Ocean (SO) circulation. In particular, the medium resolution Hadley Center Global Coupled model in CMIP6 exhibits a warm SO bias and weak Antarctic Circumpolar Current (ACC) transport. These issues are attributed to a poor representation of mesoscale eddies, which also impair the simulated transport of heat and carbon. To rectify these problems, two momentum closures (harmonic and biharmonic) are implemented in the Nucleus for European Modeling of the Ocean general circulation model: 2D Leith and Quasi-Geostrophic Leith. These Leith closures aim to capture the correct cascades of energy and enstrophy in quasi two-dimensional models. Additionally, the harmonic Leith viscosity coefficients can replace the traditional Gent-McWilliams and Redi diffusivity coefficients. In this work we explore Leith closures in an eddy-resolving channel model and an eddy-permitting forced global ocean sea-ice model, Global Ocean Sea-Ice 9 (GOSI9). The idealized model shows the Leith implementation functions as intended. In the GOSI9 configuration, the harmonic Leith schemes increase the ACC transport by 10–17%. This is in response to isopycnal flattening across Drake Passage that reduces a strong Westward flow at 60°S. This increase in ACC transport coincides with reduced warming around Antarctica and reduction of cold biases in the Atlantic. Both viscosity schemes also lead to a warm model drift. Swapping biharmonic with quasi-geostrophic Leith viscosity in GOSI9 results in one of the strongest ACC transports, along with improvements to some biases in the Atlantic.

Plain Language Summary A medium resolution climate model typically has a horizontal grid spacing of around 25 km. Compared with low-resolution models (grid spacing of 100 km), these models offer greater representation of physical processes, from low- and mid-latitude mesoscale eddies to high-latitude ice-ocean interactions. However, such model grids struggle to fully capture the dynamics of mesoscale eddies, particularly in the Southern Ocean (SO) and North Atlantic, where complex water mass transformations take place that drive the global overturning circulation. For example, the UK's medium resolution coupled model simulates a too warm SO and too weak volume transport through Drake Passage, which prevents the model from accurately predicting the response of the climate system to some aspects of anthropogenic forcing. In this study we focus on improving the representation of mesoscale eddies in this class of model by implementing two viscosity parameterizations. The impact of the viscosity parameterizations are then examined in a realistic global ocean sea-ice model. Our findings show that the parameterizations lead to an increase in Drake Passage transport and reduction in SO warming.

Key Points:

- The 2D and quasi-geostrophic (QG) Leith closures are implemented in the Nucleus for European Modeling of the Ocean and explored in an idealized channel model and the UK Met Office Global Ocean Sea-Ice 9 configuration
- Leith schemes lead to an increase in volume transport through Drake Passage, moving from ~130 Sv to the range of 140–150 Sv
- QG Leith viscosity improves the Antarctic warm bias and Atlantic cool bias, whilst the Atlantic Meridional Overturning Circulation remains within observations

Correspondence to:
T. Wilder,
t.m.wilder@reading.ac.uk

Citation:
Wilder, T., & Kuhlbrodt, T. (2025). Examining the fidelity of Leith subgrid closures for parameterizing mesoscale eddies in idealized and global (NEMO) ocean models. *Journal of Advances in Modeling Earth Systems*, *17*, e2025MS004950. https://doi.org/10.1029/2025MS004950

Received 13 JAN 2025
Accepted 29 AUG 2025

Author Contributions:
Conceptualization: T. Wilder, T. Kuhlbrodt
Data curation: T. Wilder
Formal analysis: T. Wilder, T. Kuhlbrodt
Funding acquisition: T. Kuhlbrodt
Investigation: T. Wilder, T. Kuhlbrodt
Methodology: T. Wilder, T. Kuhlbrodt
Software: T. Wilder
Supervision: T. Kuhlbrodt
Visualization: T. Wilder
Writing – original draft: T. Wilder, T. Kuhlbrodt

© 2025 The Author(s). Journal of Advances in Modeling Earth Systems published by Wiley Periodicals LLC on behalf of American Geophysical Union. This is an open access article under the terms of the Creative Commons Attribution License, which permits use, distribution and reproduction in any medium, provided the original work is properly cited.

1. Introduction

Climate modeling centers use Earth System Models (ESMs) as a primary tool to expand our knowledge of the Earth System and identify future regional and global climate change patterns. The IPCC utilize data from ESMs to form global emission targets aimed at limiting the rise in global temperatures (Calvin et al., 2023). Accurate climate change projections are in part achieved through models that can simulate realistic transports of heat and carbon. In particular, the ocean circulation plays a key role in transporting these properties throughout the Earth System, with the Southern Ocean (SO) contributing significantly to the heat and carbon budgets (Frölicher et al., 2015; Sallée et al., 2012; R. Williams et al., 2024). Moreover, the SO is the location of water mass transformations that fuel the global overturning circulation (Abernathey et al., 2016; J. Marshall & Speer, 2012). Despite the SO's importance, the eddy-permitting Hadley Center Global Coupled model version 3.1 (HadGEM GC3.1) (K. Williams et al., 2018) in CMIP6 displayed sub-standard circulation in this region (Beadling et al., 2020), attributed to the poor representation of mesoscale eddies (Storkey et al., 2025). These problems hinder the models ability to predict many aspects of the global climate's response to changes in greenhouse gas emissions.

Most ESMs use a coarse horizontal grid spacing (~1°) due to their low computational cost and freedom to explore multiple parameter spaces over centennial timescales. Low resolution models have been, and still are, excellent tools in projecting climate change. Nevertheless, higher resolution climate models in the eddy-permitting regime (~0.25°) enable more processes to be resolved. For example, low- and mid-latitude mesoscale processes are represented, which are vital for the transport and air-sea exchange of heat, carbon, and other biogeochemical tracers (Gille, 2003; Pezzi et al., 2021; Stewart & Thompson, 2015; Zhai & Greatbatch, 2006). At high latitudes, a better representation of mixing processes (Couto et al., 2017; Evans et al., 2023), transport pathways (Shan et al., 2024) and water mass transformations (Vernet et al., 2019) can be made, which are critical for coupling ESMs to dynamical ice sheets (Smith et al., 2021) and thus reducing the uncertainty in sea level and global mean temperature changes. At the same time, eddy-permitting models sit in the *numerical gray zone* (Hewitt et al., 2020), a regime where it is difficult to capture mesoscale processes over the entire grid. This is because the grid size can resolve these processes at low and mid-latitudes, but at high-latitudes a parameterization is required to represent subgrid processes. The difficulty in this regime lies in avoiding competition between resolved and parameterized processes.

The UK's medium resolution contribution to CMIP6, HadGEM3 GC3.1 MM (N216ORCA025) utilizes the Nucleus for European Modeling of the Ocean (NEMO) ocean model (Madec et al., 2019) and the Global Ocean 6.0 configuration (Storkey et al., 2018). The coupled model was submitted to various CMIP6 model intercomparison projects (Sellar et al., 2020). Several other climate modeling centers employ the NEMO ocean model, notably CNRM and IPSL (Boucher et al., 2020; Voldoire et al., 2019). In CMIP6, the SO circulation in N216ORCA025 was deemed poor, and made apparent when compared with the low-resolution models HadGEM3 GC3.1 LL (N96ORCA1) and UKESM1.0 (Sellar et al., 2019). Specifically, there is a deep warm bias and cold Antarctic Shelf bias, along with a too weak Antarctic Circumpolar Current (ACC) transport at only ~50 Sv (Kuhlbrodt et al., 2018; Roberts et al., 2019). The weak ACC transport is characterized by a too strong westward counter-flow along the Antarctic Shelf back through Drake Passage, counteracting the main eastward flow (Beadling et al., 2020). The implications of this are profound deficiencies in the simulation of heat, carbon, and other biogeochemical budgets within the ocean. Strong biases were also shown in the North Atlantic (NA), a region of great importance for deep water formation (Bullister et al., 2013). Roberts et al. (2019) highlighted warm and saline biases in the NA, while Moreno-Chamarro et al. (2022) found this to be a result of excessive deep ocean mixing.

In response to the poor performance of N216ORCA025, work has been ongoing to improve the eddy-permitting ocean component of this model, ORCA025. Guiavarc'h et al. (2025) detail the development of a new configuration, Global Ocean Sea-Ice 9 (GOSI9), which enhances the SO circulation. The developments made in this configuration were termed the *Southern Ocean Package* (SOP), which include a scale-aware Gent-McWilliams eddy parameterization and a partial slip lateral boundary condition. These developments have produced promising results in forced configurations. The net eastwards flow through Drake Passage has been increased and slight improvements are made in the NA with a decrease in the AMOC alongside a reduction in the warm bias. Storkey et al. (2025) report similar findings in HadGEM3 coupled model experiments that apply the GOSI9 development, with a more detailed focus on the SO region. In particular, the eddy-permitting model fails to accurately represent much of the along isopycnal mixing on the Antarctic shelf, leading to an overly active Antarctic Slope Current that impedes the exchange of water masses.

One of the reasons cited by both Guiavarc'h et al. (2025) and Storkey et al. (2025) for the poor SO circulation is the misrepresentation of mesoscale processes. Indeed, simulations of the SO circulation have previously been shown to be sensitive to the choice of eddy parameterization (Downes et al., 2018; Kuhlbrodt et al., 2012), while poorly parameterized mesoscale processes are a major cause of climate sensitivity in ESMs (Fox-Kemper et al., 2019). One of the main objectives of this current work is to explore alternative methods of capturing mesoscale eddy dynamics in models at grid resolutions that do not wholly resolve their physics.

Earth System Models can be treated as quasi-two dimensional due to the ocean's strong stratification (Gill, 1982); because of this we can consider methods that capture two-dimensional turbulence in eddy-permitting regimes. The turbulence closure should describe the transfer of energy between spatial and temporal scales in response to non-linear interactions. The large-scale wind field builds up available potential energy in the circulation that is

19422466, 2025, 9, Downloaded from https://agupubs.onlinelibrary.wiley.com/doi/10.1029/2025MS004950 by NICE, National Institute for Health and Care Excellence, Wiley Online Library on [16/12/2025]. See the Terms and Conditions (https://onlinelibrary.wiley.com/terms-and-conditions) on Wiley Online Library for rules of use; OA articles are governed by the applicable Creative Commons License

released by baroclinic instabilities at scales close to the first baroclinic deformation radius (Chelton et al., 1998). This transfer to smaller scales is called the forward cascade of energy, which generates mesoscale eddies. The release of potential energy is parameterized by the Gent-McWillians (GM) scheme (Gent & McWilliams, 1990), which is often used in models that do not resolve eddies. Energy can also transfer further downscale below the deformation radius, forming submesoscale eddies (Schubert et al., 2020). At even smaller scales, energy is eventually dissipated. At the first baroclinic Rossby radius of deformation, energy undergoes a conversion to barotropic energy through barotropisation, or is transferred upscale through an inverse cascade (Scott & Wang, 2005). In numerical models, the question of how to represent the energy cascade at the grid-scale is an ongoing challenge.

In GOSI9, the ORCA025 model employs a grid-scale dependent biharmonic turbulence closure that dissipates energy at the smallest scales and maintains numerical stability. The use of biharmonic friction has been shown to be important for the flux of momentum across the ACC (Gille, 1997). Megann and Storkey (2021) examine numerical mixing in ORCA025 using several viscosity schemes available in NEMO. They found that numerical mixing, temperature bias drifts, and the rate of spin down of the ACC reduced when increasing viscosity, with the biharmonic Smagorinsky (Griffies & Hallberg, 2000; Smagorinsky, 1963) displaying the best results. Despite these improvements, the Smagorinsky viscosity is only appropriate for models that resolve the inertial range of three-dimensional turbulence (Leith, 1996), which global ocean models like ORCA025 do not do. Using the Smagorinsky viscosity in eddy-permitting models leads to over dissipation of grid-scale energy and puts a halt on the 2D or QG inverse energy cascade (Bachman et al., 2017). However, there are a limited number of subgrid viscosity schemes available in NEMO, and the Smagorinsky viscosity is the best current candidate in eddy-permitting models as argued by Megann and Storkey (2021).

A viscosity parameterization more suited to large-scale ocean modeling is the Leith subgrid scheme (Leith, 1996). Like the Smagorinsky scheme, the Leith scheme is a flow- and scale-aware viscosity scheme. The Leith scheme differs from other subgrid viscosity schemes in that it dissipates enstrophy rather than energy in two-dimensional turbulence. This ensures there is a forward cascade of enstrophy and an inverse cascade of energy, as outlined in two-dimensional turbulence theory (Tabeling, 2002). Fox-Kemper and Menemenlis (2008) implemented various Leith schemes in a general circulation model, showing that modifications are necessary to maintain numerical stability. Extensions to the Leith scheme have been made to account for the quasi-geostrophic (QG) turbulence regime (Bachman et al., 2017). The QG Leith scheme can also be used to compute GM and Redi diffusivity coefficients in a QG regime. At the eddy-permitting resolution, Bachman et al. (2017) argue that the Leith contribution to the GM isopycnal flattening does not compete with the resolved eddy processes and therefore does not deplete resolved eddies. Both Leith schemes were implemented in a global ocean model at 1/10° (Pearson et al., 2017), where they were found to capture more energy below the deformation radius, while reducing interior dissipation. In the work by Bachman et al. (2017) it was noted that at eddy-permitting resolution the Leith closures may be at their limit of application, where the enstrophy cascade is not resolved or only permitted.

In this work we describe our findings from implementing the Leith subgrid eddy closures across idealized and realistic NEMO configurations. In Section 2 we present the theory behind the Leith subgrid schemes. The model configurations are described in Section 3. Using an idealized channel model, the Leith viscosity coefficients are closely explored through their contributing terms, as well as their effect on kinetic energy (KE) (Section 4). Following this, the Leith schemes are applied in a forced global ocean model to assess their effect on large-scale circulation features such as the ACC transport and SO MOC (Section 5). In the concluding Section 6, we make a recommendation to the reader and discuss future avenues of work.

2. Theory

2.1. Three-Dimensional Turbulence

Although we are not considering the Smagorinsky scheme in this work (see Megann and Storkey (2021) for an examination in a similar model configuration), it is useful to present some of the theory behind this scheme to understand how it differs to the Leith subgrid scheme, which we present in Section 2.2.

The Smagorinsky viscosity scheme (Smagorinsky, 1963) is based on a fully three-dimensional turbulence regime where horizontal and vertical scales are similar ($\Delta z \sim \Delta s$) and the Reynolds number ($\mathrm{Re} = UL/\nu$) is large. In this regime exists an inertial range where energy cascades from large to small scales through nonlinear

19422466, 2025, 9, Downloaded from https://agupubs.onlinelibrary.wiley.com/doi/10.1029/2025MS004950 by NICE, National Institute for Health and Care Excellence, Wiley Online Library on [16/12/2025]. See the Terms and Conditions (https://onlinelibrary.wiley.com/terms-and-conditions) on Wiley Online Library for rules of use; OA articles are governed by the applicable Creative Commons License

interactions. The inertial range are wavenumbers between an energy injection and energy dissipation scale. Based on the work of Kolmogorov (1941), the energy spectrum in the inertial range is

$$E(k) = K\epsilon^{2/3}k^{-5/3} \tag{1}$$

where K is the Kolmogorov constant, ϵ is the energy dissipation rate, and k is the spatial wavenumber where energy transfers to smaller scales. The wavenumber where energy is dissipated is given by Vallis (2017):

$$k_d = \epsilon^{1/4}\nu^{-3/4} \tag{2}$$

where ν is the molecular viscosity. Smagorinsky (1963) proposed a rate of energy dissipation to be proportional to the local deformation rate, D,

$$\epsilon = \nu|D|^2 \tag{3}$$

where $|D| = \sqrt{(\partial_x u - \partial_y v)^2 + (\partial_y u + \partial_x v)^2}$. By substituting the energy dissipation rate Equation 3 into Equation 2, a viscosity coefficient is defined as

$$\nu_{2S} = \left(\frac{C\Delta s}{\pi}\right)^2 |D| \tag{4}$$

where C is a dimensionless scaling parameter and the wavenumber $k_d = \pi/\Delta s$ with Δs being a measure of the grid scale. The subscript $\cdot_{2S}$ denotes harmonic Smagorinsky.

2.2. Two-Dimensional Turbulence

Since ESMs are far from the three-dimensional turbulence scale of $\Delta z \sim \Delta s$, ESMs are more appropriately considered quasi two-dimensional. In this section we introduce the theory for the two-dimensional Leith viscosity that is suggested to be more suitable for ESMs than Smagorinsky.

We begin with the two-dimensional vorticity equation

$$\partial_t q_{2d} + J(\psi, q_{2d}) = \nu\nabla^2 q_{2d} + \boldsymbol{F} \tag{5}$$

where $q_{2d} = \nabla \times \boldsymbol{u}$ is relative vorticity and $\boldsymbol{u}$ are horizontal velocities, $J(\psi, q_{2d})$ is the Jacobian, ψ is a streamfunction, ν is viscosity, and the final term on the right is forcing. The ∇ are horizontal gradients.

Energy in a two-dimensional regime depends on forcing and viscosity. With zero forcing, an energy equation takes the form

$$d_t E = \psi(\nu\nabla^2 q_{2d}) \tag{6}$$

where energy is $E = \frac{1}{2}\int_V (\nabla\psi)^2 dV$, and ν is viscosity.

In a two-dimensional turbulence cascade, energy is transferred to larger scales and enstrophy cascades to smaller scales until the cascade is halted by dissipation. Enstrophy is $Z = \frac{1}{2}\int_V q_{2d}^2 dV$. This turbulent regime is different to three-dimensional turbulence where vortex stretching contributes to the cascade of energy to smaller scales. Charney (1971) presents an alternative argument to the Kolmogorov energy spectrum used by Smagorinsky (1963). In the inertial range of two-dimensional turbulence, the energy spectrum follows the enstrophy cascade rate

$$E(k) = A\eta^{2/3}k^{-3} \tag{7}$$

19422466, 2025, 9, Downloaded from https://agupubs.onlinelibrary.wiley.com/doi/10.1029/2025MS004950 by NICE, National Institute for Health and Care Excellence, Wiley Online Library on [16/12/2025]. See the Terms and Conditions (https://onlinelibrary.wiley.com/terms-and-conditions) on Wiley Online Library for rules of use; OA articles are governed by the applicable Creative Commons License

where A is a dimensionless coefficient, and η is an enstrophy dissipation rate. A wavenumber for enstrophy dissipation is Vallis (2017):

$$k_d = \eta^{1/6}\nu^{-1/2} \tag{8}$$

A positive definite term for the enstrophy dissipation rate was estimated by Leith (1996) to be

$$\eta \approx \nu\left(\nabla q_{2d} \cdot \nabla q_{2d}\right) \tag{9}$$

Adding Equation 9 into Equation 8 and taking $k_d = \pi/\Delta s$ gives a term for viscosity

$$\nu_{2d} = \left(\frac{\Delta s \Lambda}{\pi}\right)^3 |\nabla_h q_{2d}| \tag{10}$$

where Λ is parameter that is $O(1)$. Equation 10 is the original form proposed by Leith (1996), however, additional work has been made to improve the scheme in numerical models.

The Leith viscosity scheme in Equation 10 has been shown to be unstable to horizontal divergent motions. Using the Leith viscosity, Fox-Kemper and Menemenlis (2008) found their numerical simulations became unstable and exhibited checkerboard patterns in vertical velocity. To counter this problem, they added a divergence term to Equation 10

$$\nu_{2d} = \left(\frac{\Delta s}{\pi}\right)^3 \sqrt{\Lambda_q^6 |\nabla_h q_{2d}|^2 + \Lambda_d^6 |\nabla_h (\nabla_h \cdot \boldsymbol{u})|^2} \tag{11}$$

In Equation 11, the parameters Λ_q and Λ_d can be chosen to act on gradients of vorticity and divergence, respectively. In NEMO, we implement Equation 11 as the *2D Leith* viscosity scheme. The vorticity term q_{2d} also contains the Coriolis parameter, f.

2.2.1. Extension to Quasi-Geostrophic Dynamics

The 2D Leith scheme was extended by Bachman et al. (2017) to accommodate the QG regime by employing the QG potential vorticity. The governing equations for the QG regime are the vorticity and buoyancy anomaly equations

$$\partial_t q_{2d} + \boldsymbol{u} \cdot \nabla q_{2d} - f_0 \partial_z w + \beta v = \nu \nabla^2 q_{2d} \tag{12a}$$

$$\partial_t b + \boldsymbol{u} \cdot \nabla b + w N^2(z) = D_b \tag{12b}$$

In the above: f_0 is the Coriolis parameter, w are vertical velocities, $b = f_0 \psi_z$ is the buoyancy anomaly with vertical gradient of the stream function ψ_z, N^2 is the square of the buoyancy frequency, and D_b is a term containing diffusion of temperature and salinity.

Then combining Equations 12a and 12b gives the QG potential vorticity equation

$$\partial_t q_{qg} + \boldsymbol{u} \cdot \nabla q_{qg} + \beta v = \nu \nabla^2 q_{2d} + \partial_z \frac{f_0 D_b}{N^2(z)} \tag{13}$$

where $q_{qg} = q_{2d} + \partial_z \left(f_0/N^2\right) b$ is the potential vorticity. In QG dynamics, the vortex stretching term is added to the relative vorticity to form q_{qg}. In 2D turbulence, enstrophy is fully cascaded to dissipation, while in QG turbulence the stretching term reinjects enstrophy back into the flow.

Then, similarly to 2D Leith viscosity, a *QG Leith* viscosity scheme is

19422466, 2025, 9, Downloaded from https://agupubs.onlinelibrary.wiley.com/doi/10.1029/2025MS004950 by NICE, National Institute for Health and Care Excellence, Wiley Online Library on [16/12/2025]. See the Terms and Conditions (https://onlinelibrary.wiley.com/terms-and-conditions) on Wiley Online Library for rules of use; OA articles are governed by the applicable Creative Commons License

$$\nu_{qg} = \left(\frac{\Delta s}{\pi}\right)^3 \sqrt{\Lambda_q^6 |\nabla_h q_{qg}|^2 + \Lambda_d^6 |\nabla_h (\nabla_h \cdot \boldsymbol{u})|^2} \tag{14}$$

We employ individual Λ parameters for vorticity and divergence in Equation 14 following Fox-Kemper and Menemenlis (2008). This is something that neither Bachman et al. (2017) nor Pearson et al. (2017) did, which we do to allow some flexibility for the user to ameliorate any issues of grid-scale noise in NEMO.

While the numerical implementation of the 2D Leith scheme is relatively straightforward, the QG Leith scheme requires some care. QG dynamics is valid for Burger number $\sim O(1)$, where $Bu = L_d/\Delta s$. The baroclinic deformation radius, L_d is

$$L_d = \frac{1}{|f|\pi} \int_{-H}^{0} N(z) dz \tag{15}$$

Additional dimensionless numbers are required: the Rossby number, $Ro = U/|f|\Delta s$; and the Froude number, $Fr = Ro/\sqrt{Bu}$. In Ro, U is a gridscale velocity. For regimes where the Burger number is not $O(1)$, for example, when $Bu \gg 1$ or Fr is large, the QG Leith scheme tends to the 2D Leith scheme. The following implementation achieves a smooth transition to the 2D Leith scheme through a condition imposed on the stretching term (Bachman et al., 2017):

$$S = \min\left(\left| \partial_z \frac{f}{N^2} \nabla_h b \right|, \left(\frac{|\nabla_h q_{2d}| Fr^2}{Ro^2 + Fr^4} \right) \right) \tag{16}$$

Equation 16 ensures that the QG Leith scheme will always scale to the 2D Leith when QG dynamics are not valid. Following Pearson et al. (2017), we omit the calculation of the QG Leith scheme in the mixed layer due to the absence of N^2 vertical gradients.

2.3. A Leith-Like Biharmonic Viscosity

Following Griffies and Hallberg (2000), a Leith-like biharmonic viscosity coefficient can take the form

$$\nu_4 = \nu_2 \frac{\Delta s^2}{8} \tag{17}$$

which is set according to stability constraints (Griffies, 2004). By implementing a Leith-like biharmonic viscosity, greater scale selectivity is achieved over a laplacian viscosity, where a laplacian operator will dampen longer wavelengths faster than a bilaplacian. The biharmonic operator allows the large-scale ocean circulation to evolve more freely while the small scales are dissipated. The reader should refer to Fox-Kemper and Menemenlis (2008) for a full Biharmonic Leith formulation, which we do not implement here.

2.4. A Note on 2D and QG Dissipation

In the formulation of the 2D Leith viscosity in Section 2.2, the dissipation mechanism is produced by the viscosity on vorticity (see Equation 5). This action leads to a sink of KE. In QG dynamics, combining the QG vorticity Equation 12a and buoyancy anomaly Equation 12b equation introduces buoyancy diffusion which acts to dissipate potential energy. The QG Leith viscosity scheme will dissipate both kinetic and potential energy.

2.5. Leith Viscosity Coefficient as Eddy and Tracer Diffusion

Sub-gridscale mesoscale eddy processes are parameterized in non eddy-resolving models using a formulation of the Gent et al. (1995) (GM) scheme. The GM parameterization introduces an additional velocity term to the tracer advection equation to represent the effect mesoscale eddies have on the mean circulation. A choice of a coefficient κ_{gm} is made to inform isopycnal flattening by eddies, with various GM coefficients proposed (Ferreira et al., 2005; Mak et al., 2017, 2018; D. Marshall et al., 2012; Treguier et al., 1997; Visbeck et al., 1997). In the work of Bachman et al. (2017) they additionally worked through the proposition of ν_{2d} or $\nu_{qg} = \kappa_{gm}$, and similarly for a

19422466, 2025, 9, Downloaded from https://agupubs.onlinelibrary.wiley.com/doi/10.1029/2025MS004950 by NICE, National Institute for Health and Care Excellence, Wiley Online Library on [16/12/2025]. See the Terms and Conditions (https://onlinelibrary.wiley.com/terms-and-conditions) on Wiley Online Library for rules of use; OA articles are governed by the applicable Creative Commons License

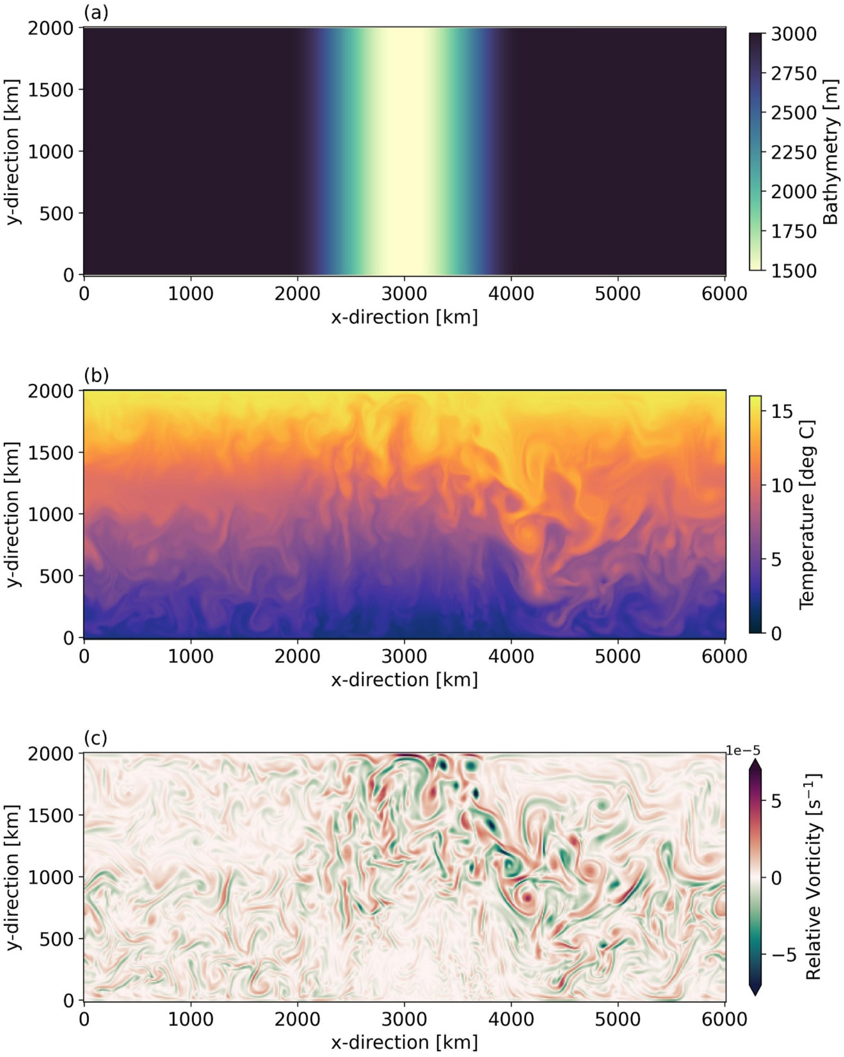

Figure 1. Idealized channel model. In panel (a) bathymetry, and at simulation year 51, (b) temperature at 5 m, and (c) relative vorticity at 5 m.

tracer diffusion, κ_{redi}. In this work we run simulations by setting the GM and Redi diffusivity as the Leith viscosity coefficient.

3. Model and Experimental Setup

In this study we examine the Leith schemes in both idealized and realistic configurations. To do this we employ the Nucleus for European Modeling of the Ocean (NEMO) (Madec et al., 2019) at version 4.0.4. In the idealized case we look to represent the dynamics of the SO using an idealized channel model (Mak, 2023), also similar to other studies (Abernathey et al., 2011; Munday et al., 2015). In the realistic case, we use a forced global ocean sea-ice configuration, GOSI9 (Guiavarc'h et al., 2025). Below, we describe each in detail.

3.1. Channel Model

The idealized model is a zonally re-entrant channel model with a domain spanning 2,000 km meridionally and 6,000 km zonally, and has walls at the north and south side. The model uses a z-coordinate system with partial steps. It has a depth of 3,000 m with 30 vertical levels and spacing of 10 m near the surface, increasing with depth. The horizontal grid spacing is 10 km, which is sufficient to resolve the largest of eddies within the domain (see Figure 3d). Centered at 3,000 km in the *x*-direction, there is a submerged Gaussian bump of 1,500 m in height

19422466, 2025, 9, Downloaded from https://agupubs.onlinelibrary.wiley.com/doi/10.1029/2025MS004950 by NICE, National Institute for Health and Care Excellence, Wiley Online Library on [16/12/2025]. See the Terms and Conditions (https://onlinelibrary.wiley.com/terms-and-conditions) on Wiley Online Library for rules of use; OA articles are governed by the applicable Creative Commons License

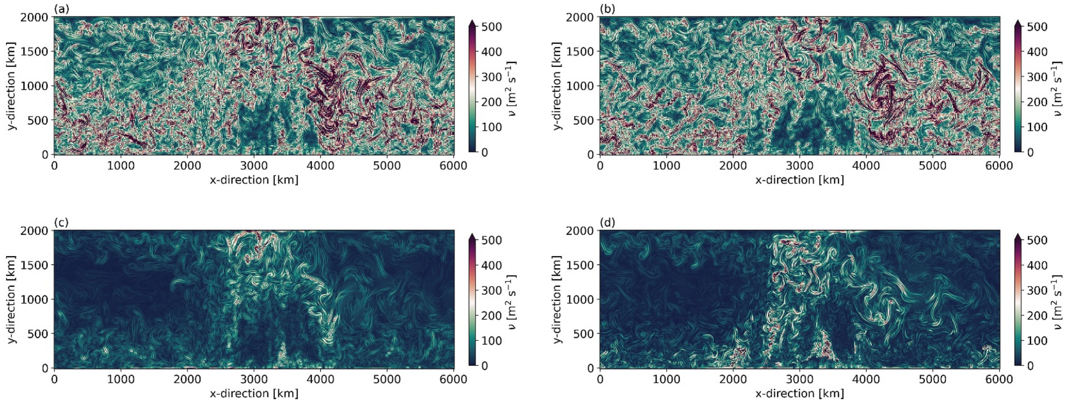

Figure 2. Harmonic 2D Leith (a, c) and QG Leith (b, d) viscosity at 5 m (top panels) and 1,400 m (bottom panels). Data are instantaneous snapshots at simulation year 51.

from the ocean bottom (Figure 1a). The model is setup on a β plane where 50°S is at 1,000 km in the y-direction. For advection, momentum uses a second order centered vector form scheme and tracers employ a centered scheme of fourth order in the horizontal and second order in the vertical.

The model is initialized with a temperature profile similar to Abernathey et al. (2011) that takes the form

$$T(x,y,z) = (1+\Delta T(y/L_y))(\exp(z/h) - \exp(-H/h))/(1-\exp(-H/h)), \tag{18}$$

where L_y is the length of the domain in the y-direction and z is the depth at each vertical level. In Equation 18, the temperature profile increases linearly south to north with $\Delta T = 15$°C, and exponentially decays with an e-folding height scale of $h = 1000$ m to the ocean bottom, H. A surface temperature restoring condition is also applied. At the Northern boundary, there is a temperature sponge layer of width 100 km that has a restoring timescale of 7 days at the domain edge decreasing to zero restoring at 1,900 km. The model is forced by a wind profile prescribed by

$$\tau_s(y) = \tau_0 \sin(\pi y/L_y) \tag{19}$$

where $\tau_0 = 0.2$ N m^{-2} and has a peak forcing at $L_y/2$. We use absolute wind stress, meaning we omit the interaction between wind speed and ocean current. Bottom stress is non-linear and assumes a quadratic form

$$\tau_b = C_D \boldsymbol{u}_b^2 \tag{20}$$

where the drag coefficient is $C_D = 1.1 \times 10^{-3}$, and $\boldsymbol{u}_b$ is the ocean velocity in the bottom layer.

The model is spun up for 50 years, although this is quite short compared to the 620 years employed by Munday et al. (2015), we find that after only a few model years, the volume integrated KE reaches a steady state. Since the purpose of this idealized channel model is to assess whether the Leith schemes are technically implemented correctly, the 50 year spin up is adequate. A further simulation year is carried out for analysis with 5 daily mean and instantaneous outputs.

In the Leith formulations of Pearson et al. (2017) and Bachman et al. (2017), they used $\Lambda = 1.0$. In our work we increase this parameter to $\Lambda = 2.0$ for harmonic and $\Lambda = 2.6$ for biharmonic in order to reduce levels of noise. Ilıcak (2016) noted that the Leith schemes tend to have higher levels of numerical mixing than the Smagorinsky scheme. In the biharmonic case, the larger Λ is chosen so the Leith scheme has comparable levels of viscosity with the grid-aware biharmonic case. Munday et al. (2015) and Yang et al. (2022) also use a tunable parameter larger than 1.0.

19422466, 2025, 9, Downloaded from https://agupubs.onlinelibrary.wiley.com/doi/10.1029/2025MS004950 by NICE, National Institute for Health and Care Excellence, Wiley Online Library on [16/12/2025]. See the Terms and Conditions (https://onlinelibrary.wiley.com/terms-and-conditions) on Wiley Online Library for rules of use; OA articles are governed by the applicable Creative Commons License

Table 1
Idealized Simulations

Viscosity	Simulation name	GM/Redi Leith
Biharmonic	biharm	No
Harmonic 2D Leith	harm_2dleith_2.0	No
Harmonic QG Leith	harm_qgleith_2.0	No
Harmonic 2D Leith	harm_2dleith_2.0_gm	Yes
Harmonic QG Leith	harm_qgleith_2.0_gm	Yes
Biharmonic 2D Leith	biharm_2dleith_2.6	No
Biharmonic QG Leith	biharm_2dleith_2.6	No

Note. Harmonic Leith use $\Lambda = 2.0$; Biharmonic Leith uses $\Lambda = 2.6$.

3.2. Global Model

The global model uses the GOSI9 configuration (Guiavarc'h et al., 2025). This is an iteration of previous global ocean configurations (Storkey et al., 2018), and now forms part of the Met Office Hadley Center Global Coupled model version 5 (Xavier et al., 2023). The GOSI9 configuration is comprised of the NEMO ocean model at version 4.0.4 and the sea ice model SI^3 (Blockley et al., 2023). In this work we use the GOSI9 version at 0.25° on the ORCA grid, which is termed ORCA025. The ORCA025 grid is eddy-permitting with horizontal grid lengths of 25 km near the equator and 6 km at higher latitudes, enabling the resolving of some mesoscale processes beyond the 1° ORCA1 version. In the following, we describe some pertinent details for the reader, but encourage anyone interested to read the description of GOSI9 in Guiavarc'h et al. (2025).

In the standard GOSI9 version, mixing of momentum is achieved through a grid-scale aware biharmonic closure, with values ranging from 1.1×10^{11} m^4 s^{-1} near the equator to 3.5×10^9 m^4 s^{-1} in high latitudes. Diffusion of tracers is carried out along isopycnals through a harmonic grid-aware scheme and has a coefficient of 150 m^2 s^{-1} at the equator. Vertical mixing of tracers and momentum is parameterized using a modified Turbulent KE scheme (Gaspar et al., 1990).

One of the key developments of GOSI9 has been the development of the SOP (Guiavarc'h et al., 2025; Storkey et al., 2025). The SOP includes a scale aware GM eddy parameterization and a partial slip lateral boundary condition south of 50°S. Previous versions of the Global Ocean configuration like GO6 did not use any mesoscale eddy parameterizations at eddy-permitting resolution. The GM eddy parameterization in the SOP is based on Hallberg (2013), whereby the GM advection coefficient κ_{gm}, is set as a function of the Rossby radius of deformation L_d (Storkey et al., 2025):

$$\kappa_{gm} = \min\left(1.0, \frac{2}{3}(2.0 - L_d/\Delta s)\right) \times 75.0 \text{ m}^2 \text{ s}^{-1} \tag{21}$$

Equation 21 implies $\kappa_{gm} = 0$ when $L_d/\Delta s > 2$ and ramps up linearly to 75.0 m^2 s^{-1} when $L_d/\Delta s = \frac{1}{2}$. The partial slip south of 50°S is intended to increase topographic drag to dampen overactive SO gyres. We note that the introduction of SOP modified the tracer advection scheme from second to fourth order, however, we have not modified this aspect, retaining fourth order for all simulations.

In terms of our experimental simulations, the GOSI9 configuration in Guiavarc'h et al. (2025) is termed the reference, with each modification to the reference appropriately labeled (see Table 2 for simulations). Four simulations neglect a form of GM: biharm_noSO, harm_2dleith_2.0_nSO, harm_qgleith_2.0_nSO, biharm_2dleith_2.6_nSO. We carried out a total of nine simulations over two integration periods: a 30 year spin up, followed by a 34 year analysis cycle. The spin up run is initialized from EN4 climatology (Good et al., 2013). Each cycle employs CORE-II forcing starting at year 1976, recycling the forcing on the second cycle and extending to 2009. Other modeling centers show that many key climate metrics do not reach equilibrium after one cycle, sometimes taking five full cycles (Adcroft et al., 2019).

In the standard GOSI9 configuration a time-step of 1,800 s is employed. It was found that by employing the same tuneable parameters in Leith as in the idealized case, the model tended to crash owing to stability issues. It was shown by Megann and Storkey (2021) that increasing viscosity in GO6 required a reduction in time-step. When running the Leith schemes we have used a time-step of 1,200 s to maintain numerical stability.

4. Results: Idealized Channel Model

We present the first set of results by exploring seven idealized channel model simulations. The simulations are summarized in Table 1. We describe the contributions to the Leith viscosity coefficients and their impact on the models KE.

19422466, 2025, 9, Downloaded from https://agupubs.onlinelibrary.wiley.com/doi/10.1029/2025MS004950 by NICE, National Institute for Health and Care Excellence, Wiley Online Library on [16/12/2025]. See the Terms and Conditions (https://onlinelibrary.wiley.com/terms-and-conditions) on Wiley Online Library for rules of use; OA articles are governed by the applicable Creative Commons License

19422466, 2025, 9, Downloaded from https://agupubs.onlinelibrary.wiley.com/doi/10.1029/2025MS004950 by NICE, National Institute for Health and Care Excellence, Wiley Online Library on [16/12/2025]. See the Terms and Conditions (https://onlinelibrary.wiley.com/terms-and-conditions) on Wiley Online Library for rules of use; OA articles are governed by the applicable Creative Commons License

Table 2
ORCA025 Simulations

Viscosity	Simulation name	GM/Redi Leith	SOP
Biharmonic	biharm	No	Yes
Harmonic 2D Leith	harm_2dleith_2.0	No	Yes
Harmonic QG Leith	harm_qgleith_2.0	No	Yes
Biharmonic	biharm_nSO	No	No
Harmonic 2D Leith	harm_2dleith_2.0_nSO	No	No
Harmonic QG Leith	harm_qgleith_2.0_nSO	No	No
Harmonic 2D Leith	harm_2dleith_2.0_gm	Yes	No
Harmonic QG Leith	harm_qgleith_2.0_gm	Yes	No
Biharmonic 2D Leith	biharm_2dleith_2.6_nSO	No	No

Note. Harmonic Leith use $\Lambda = 2.0$; Biharmonic 2D Leith uses $\Lambda = 2.6$.

4.1. Description of Harmonic Leith Viscosity

The harmonic Leith viscosity coefficient fields are shown in Figure 2 for simulations harm_2dleith_2.0 and harm_qgleith_2.0. At the 5 m depth level, the 2D and QG Leith fields are qualitatively similar (Figures 2a and 2b). The similarity in surface fields is due to QG Leith scaling to 2D Leith within the mixed layer. At approximately 1,400 m, a difference between the Leith fields becomes evident. The additional stretching term increases the QG Leith viscosity coefficient, defining more eddy-like features in the flow. This increase becomes most apparent as the flow begins to pass the ridge at 3,000 km in the x-direction.

Terms that contribute to the QG Leith viscosity coefficient at a depth of $\sim$529 m are shown in Figure 3. Large horizontal vorticity gradients appear over the ridge at 3,000 km zonally and downstream (Figure 3b), consistent with increased eddy activity downstream of topographic features (e.g., Figure 2 in Youngs et al. (2017)). The stretching term (Figure 3c) follows the main flow pattern as it passes the ridge, following the f/H contour (D. Marshall, 1995). The contour overlaying the stretching field is the Burger number interval, $Bu \in (0.5, 2) \sim O(1)$. When $Bu \sim O(1)$, and both Ro and Fr are small (Figures 3e and 3f), the flow lies in the QG regime. Within this Burger number interval the stretching term is not negligible and contributes to the viscosity coefficient (Figure 3a). North of the $Bu = 2$ contour line, stretching values become smaller, and QG Leith tends to the 2D Leith as Bu gets large. To the south of the $Bu = 0.5$ contour line, the stretching term is not computed in some regions due to the depth level of 529 m still being in the mixed layer in some places. Just below the mixed layer, large vertical gradients in N^2 produce large stretching values.

4.2. Comparison of Leith Schemes—Impact on Kinetic Energy

The harmonic Leith viscosity coefficients, horizontally averaged over the domain, are displayed in Figure 4a. The QG Leith schemes have larger coefficients on average than the 2D Leith as a result of the stretching term. There is

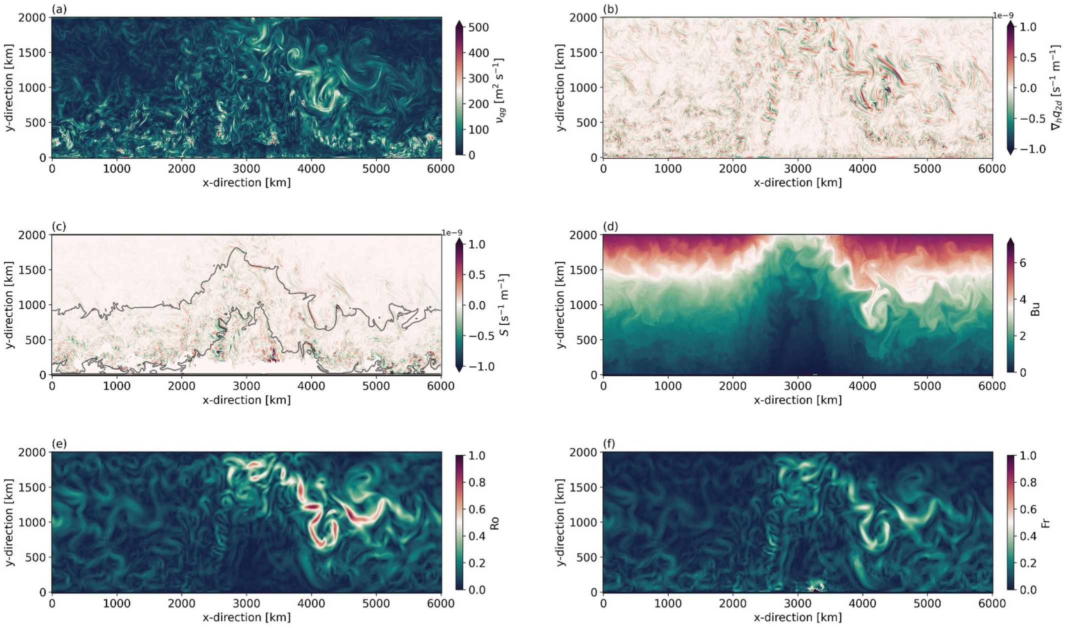

Figure 3. Contributing terms to the harmonic quasi-geostrophic (QG) Leith viscosity field at 529 m. In panel (a) QG Leith viscosity coefficient, (b) horizontal gradient of relative vorticity, (c) quasi-geostrophic stretching, (d) Burger number $Bu = L_d/\Delta s$, (e) Rossby number $Ro = U/|f|\Delta s$, and (f) Froude number $Fr = Ro/\sqrt{Bu}$. Data are instantaneous snapshots at simulation year 51.

19422466, 2025, 9, Downloaded from https://agupubs.onlinelibrary.wiley.com/doi/10.1029/2025MS004950 by NICE, National Institute for Health and Care Excellence, Wiley Online Library on [16/12/2025]. See the Terms and Conditions (https://onlinelibrary.wiley.com/terms-and-conditions) on Wiley Online Library for rules of use; OA articles are governed by the applicable Creative Commons License

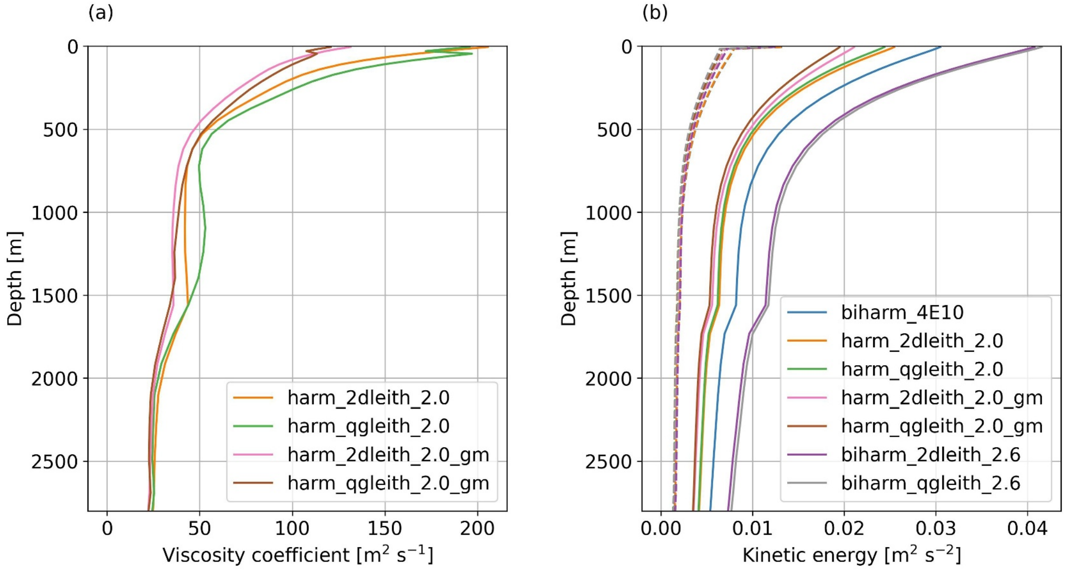

Figure 4. Horizontal average of (a) harmonic Leith viscosity coefficient, and (b) mean (dashed) and eddy (full) kinetic energy. Simulations suffixed with gm include iso-neutral diffusivity. Data is computed from simulation year 51.

a sharp increase in viscosity in the QG Leith case where the scheme transitions below the mixed layer. When the Leith schemes are used as the GM advection and Redi diffusion coefficients (harm_2dleith_2.0_gm and harm_qgleith_2.0_gm), the average viscosity coefficient is smaller. This decrease is quite clear at the surface where there is around a 25% reduction.

Figure 4b shows the horizontal average of mean (MKE) and eddy kinetic (EKE) energy across all idealized simulations, including Leith-like biharmonic. In each of MKE (dashed line) and EKE (full line), the vertical profiles are similar, with the largest values near the surface. At 1,600 m depth there is a decrease associated with the topographic ridge peak, most prominent in EKE. MKE profiles are almost the same across simulations. Looking at the EKE profiles, the harmonic Leith cases display the weakest EKE, while the biharmonic Leith exhibits the strongest EKE, with biharm_4E10 in between. The QG Leith harmonic display weaker EKE than the 2D Leith cases. These results are similar to those observed by Grooms (2023) (see their Figure 4) who considered total KE (mean plus eddy). Weaker EKE in the harmonic cases can be explained by harmonic schemes being less scale selective than biharmonic schemes, overdamping at larger length scales (Griffies & Hallberg, 2000). The EKE with QG Leith harmonic is weaker because this scheme dissipates available potential energy, while the 2D Leith scheme only dissipates KE (see Section 2). The Leith plus GM runs have the weakest EKE and is a result of the GM scheme acting as a further sink of potential energy, a known deficiency of GM schemes (Bachman, 2019).

Further analysis is carried out through a time-mean kinetic energy (KE) spectra at the first depth level (~5 m), displayed in Figure 5. Parts of the energy spectrum are similar to the EKE vertical profiles in Figure 4b, but we can now see how each simulation varies across length scales. Between 30 and 20 km $\left(k > 10^{-1}\right)$ the KE spectra resemble the vertical EKE profiles. In this range the Leith plus GM runs have the weakest energy, while the biharmonic Leith-like schemes have the greatest. Approaching the grid-scale at 10 km, the biharm_4E10 simulation has the weakest energy, while Leith plus GM accumulates more energy, perhaps owing to the weaker viscosity coefficients (Figure 4a). In addition, the biharmonic viscosity types all have steeper spectra compared with harmonic Leith, which follow more closely the k^{-3} spectra at this scale. Bachman et al. (2017) showed shallower spectral slopes for harmonic Leith at the eddy-permitting/resolving resolution, though a reason for our steeper slopes could be due to our choice of $\Lambda = 2.0$.

5. Results: Forced Global Ocean Model

One of the primary objectives of this work is to improve NEMO's simulation of the SO in ORCA025. In addition, we explore effects in the NA due to the connectivity between the two ocean basins. We document our findings

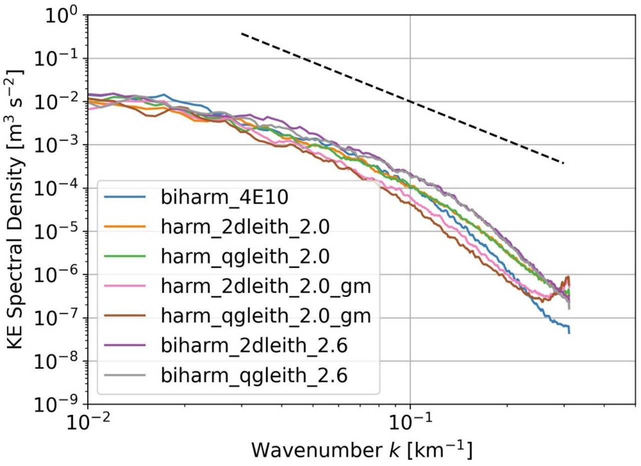

Figure 5. Kinetic energy spectra at 5 m depth time-averaged and smoothed with a moving average of window size 3. Dashed line is a k^{-3} slope spanning 100 km down to the grid-scale, 10 km. Simulation suffixed with gm includes iso-neutral diffusivity. Data is computed from simulation year 51.

from nine simulations, referring to each simulation using the simulation name in Table 2. Much of the analysis is made over the second cycle over forcing years 1986–2009.

5.1. Viscosity Field

The 2D and QG Leith viscosity fields in the SOP runs (harm_2dleith_2.0 and harm_qgleith_2.0) are presented in Figure 6 over the global domain at the surface and 300 m depth. As was the case in the idealized simulations, both Leith viscosity fields at the surface are similar in space (Figures 6a and 6b). The greatest viscosities (upwards of 800 m^2 s^{-1}) are found primarily on the Western Boundaries, such as the Gulf Stream (GS), Kuroshio, and Agulhas regions. These regions are hotspots of eddy activity and are known to display high levels of eddy dissipation (Tedesco et al., 2022; Zhai et al., 2010). The viscosity coefficients here are about an order of magnitude larger than those in Pearson et al. (2017), which can be attributed to two causes: their use of eddy-resolving simulations at $1/10°$ and our use of $\Lambda = 2.0$. Across the SO there are pockets of large viscosities that correspond to the path of the ACC and downstream of topographic features, such as east of the Kerguelen Plateau at 60°E. A slight reduction in viscosity can be observed in harm_qgleith_2.0 in the NA where the NA Current flows West into the Irminger and Greenland Currents. This may indicate differences in the strength of the AMOC (see Section 5.3.1). At 300 m depth (Figures 6c and 6d) both schemes differ, with larger viscosity in harm_qgleith_2.0 due to the stretching term. The increase in viscosity is found throughout the SO, NA, and Pacific. In regions where deep mixed layers are expected, such as South of Greenland and the Weddell Gyre (Holte et al., 2017), the Leith schemes are similar since QG Leith tends to the 2D Leith formulation within mixed layers.

A vertical profile of the median viscosity coefficient is shown in Figure 7 for two sub-regions: Southern Ocean (SO) (60°−30°S); and NA (0°−60°N, 70°−0°W). Each region is broadly similar for the simulation with the largest and weakest coefficient, with the NA having larger surface and mid-depth values (Figure 7b) and the SO having larger bottom values (Figure 7a). The SO profile is similar to the global profile given in Figure 2 in Pearson et al. (2017), showing there are regional differences in viscosity. At the surface, harm_qgleith_2.0 exhibits an increase in the viscosity at depth compared with harm_2dleith_2.0, which occurs deeper in the SO than the NA. The first two solid lines in the figure legend relate to the data shown in Figure 6, which both show similar patterns and color saturation at the surface (Figure 7), as do harm_qgleith_2.0_gm and harm_2dleith_2.0_gm runs. When

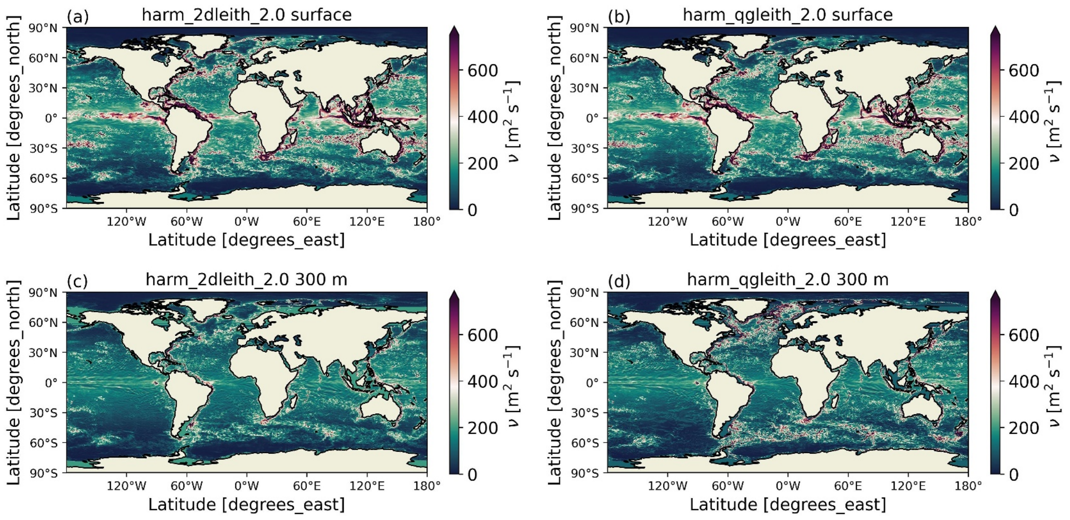

Figure 6. Harmonic 2D Leith (a, c) and quasi-geostrophic Leith (b, d) viscosity fields at surface (top panels) and 300 m (bottom panels). Data is a monthly mean taken from simulation period December 2009.

19422466, 2025, 9, Downloaded from https://agupubs.onlinelibrary.wiley.com/doi/10.1029/2025MS004950 by NICE, National Institute for Health and Care Excellence, Wiley Online Library on [16/12/2025]. See the Terms and Conditions (https://onlinelibrary.wiley.com/terms-and-conditions) on Wiley Online Library for rules of use; OA articles are governed by the applicable Creative Commons License

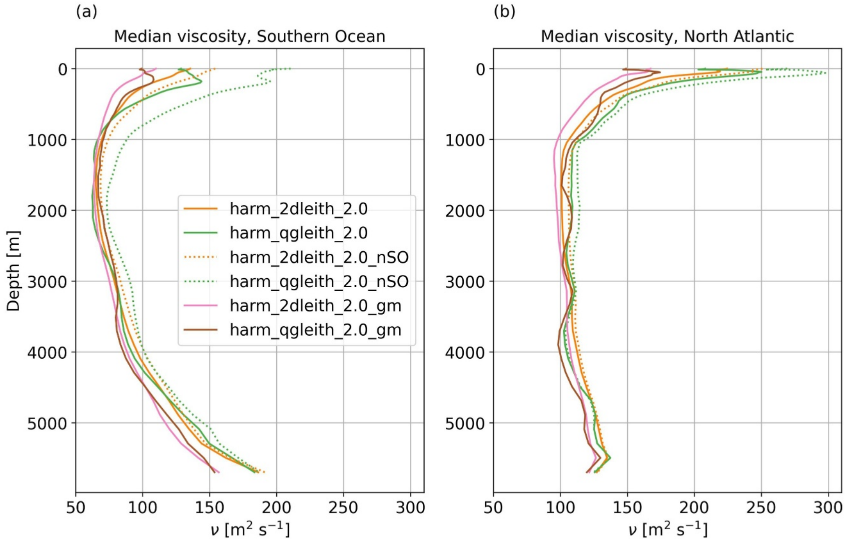

Figure 7. Median Leith viscosities computed in (a) the Southern Ocean (0°−360°E, 60°−30°S) and (b) the North Atlantic (0°−65°N, 70°−0°W). Data is computed from a time-mean taken over period 1986 − 2009 in second cycle.

Leith is used for the GM and Redi diffusivities, the viscosity coefficient is the smallest throughout much of the water column, similar to the idealized simulations shown in Figure 4a. Down the water column, the QG Leith coefficient is larger than the 2D Leith, where changes in water masses are highlighted through the wave-like patterns in QG Leith due to the stretching term.

In the SO (Figure 7a), with SOP turned off, viscosity in harm_qgleith_2.0_nSO shows a surface increase of 50 m^2 s^{-1} compared to harm_2dleith_2.0_nSO. This is despite the QG Leith tending to the 2D Leith at the surface. Between these two simulations the stretching term in QG Leith is the key difference, adding enstrophy into the flow, reflecting the forward cascade. However, the large discrepancy cannot only be because of stretching since the change is at the surface. The larger viscosity at the surface may be associated with greater surface energetics, which is not as pronounced in the NA (Figure 7b).

Since Bachman et al. (2017) proposed the viscosity coefficient for use as the GM and Redi coefficients, we will contrast the values and spatial distributions with the current tracer diffusion in GO configurations and also make comparisons with current estimates. In GOSI9 the tracer diffusivity is set to 150 m^2 s^{-1} at the equator and 30–80 m^2 s^{-1} in high latitudes. From Figure 7, we see that the values of the Leith coefficients are larger, perhaps leading to excessive tracer diffusion. Using observations, Groeskamp et al. (2020) present a surface Redi diffusivity (see their Figure 3) that is broadly similar to the viscosity coefficients shown in Figures 6a and 6b. However, there are some key differences. Focusing on the GS region, they show suppressed diffusivity near the coast and stronger diffusivity south of the mean current. This is opposite to what is shown in our results, with large coefficients hugging the coastline, and weaker values south of the GS. Mean currents are known to suppress tracer diffusivities (Klocker & Abernathey, 2014) while we would expect enhanced viscosity within the GS due to mesoscale activity. The difference here suggests a possible limitation of the Leith viscosities as Redi diffusivities. Further discrepancies are highlighted by considering the depth profile. Abernathey et al. (2010) use a SO model to show enhanced isopycnal diffusivity at mid-depth, associated with the steering level of baroclinic waves. Enhanced mixing at mid-depth is not observed in Figure 7a. Similarly, Groeskamp et al. (2020) showed strong suppression of isopycnal mixing at the surface, but not at mid-depth, in the SO. However, in the NA, the viscosity coefficient is similarly surface intensified like the diffusivity in Groeskamp et al. (2020).

5.2. Southern Ocean

In this section we focus our attention on the SO by exploring the ACC transport and meridional overturning. For the remaining results, we focus most of our attention on three simulations that exhibit some of the key differences: biharm; harm_2dleith_2.0; harm_qgleith_2.0.

19422466, 2025, 9, Downloaded from https://agupubs.onlinelibrary.wiley.com/doi/10.1029/2025MS004950 by NICE, National Institute for Health and Care Excellence, Wiley Online Library on [16/12/2025]. See the Terms and Conditions (https://onlinelibrary.wiley.com/terms-and-conditions) on Wiley Online Library for rules of use; OA articles are governed by the applicable Creative Commons License

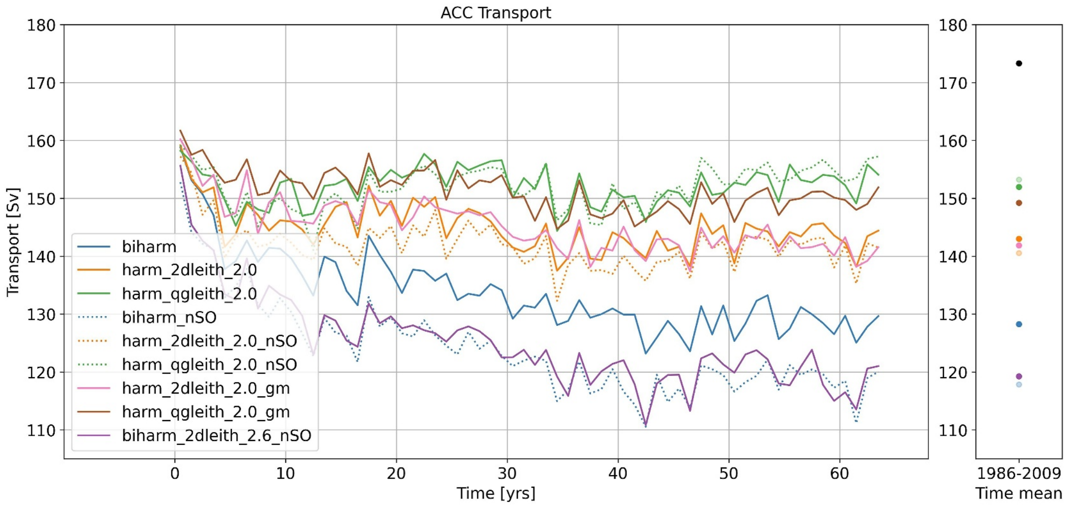

Figure 8. Time series of volume transport through Drake Passage along section 67°S−54°S, 292°E for all nine ORCA025 simulations. Data is computed for each monthly output and then yearly averaged. Right panel shows 1986−2009 time mean in the second cycle (year 40 to end), and the top most black dot denotes the estimate of Donohue et al. (2016).

5.2.1. Antarctic Circumpolar Current

Figure 8 displays the ACC transport for all simulations over two cycles (64 years in total). The transport is measured through the Drake Passage along the section 67°−54°S, 292°E. All Leith simulations, except biharm_2dleith_2.6_nSO display larger volume transport compared with biharm (reference simulation). The little change in biharm_2dleith_2.6_nSO is because the biharmonic Leith-like scheme is tuned to similar values to that of the biharmonic grid-aware scheme and may also have greater numerical mixing that degrades the ACC (Megann & Storkey, 2021). Now, comparing with biharm, the harmonic Leith schemes exhibit transports of 10−17% higher. The QG Leith simulations have the greatest transport, with a mean value just over 150 Sv (right panel), while the harmonic 2D Leith simulations have values just over 140 Sv. Consistent with this are the viscosity coefficients in the SO (Figure 7a), where QG Leith simulations have greater viscosity as a result of the increase in mean flow (ACC) strength. Interestingly, there is very little difference between each set of harmonic 2D and QG Leith simulations (e.g., with and without SOP). This shows that the viscosity scheme alone is able to reproduce similar transports without either the Leith GM/Redi diffusion or the SOP weak GM. Various observations of Drake Passage transport give values of 136−173 Sv (Cunningham et al., 2003; Koenig et al., 2014; Vargas-Alemañy et al., 2023), which certainly puts the harmonic Leith simulations within this range. However, the Leith simulations are still at least 20 Sv below the most recent recognized observational value of 173.3 Sv (Donohue et al., 2016), though Vargas-Alemañy et al. (2023) point out that volume estimates vary depending on the choice of section.

Zonal velocities through Drake passage in NEMO models were shown by Beadling et al. (2020) to contain considerable return (western) flow, which was also illustrated in Guiavarc'h et al. (2025). Figure 9 displays the zonal velocity and density contours across the Drake passage section (67°−54°S, 292°E). The simulation data is presented as the 1986–2009 time average from the second cycle. The biharm simulation is shown in Figure 9a, displaying strong eastward and westward currents to the north with poorly defined isopycnal slopes when compared to climatology (Figure 9f). When the Leith viscosity schemes are used (Figures 9b and 9c), there is a reduction in the return flow north of 60°S, with the greatest reduction in harm_qgleith_2.0. From biharm to harm_qgleith_2.0, there is also a slight reduction in the overall magnitude and width of the jet in the eastward flow in the north due to a flattening of isopycnal slopes. Moreover, in this region the surface viscosity coefficients are large (Figures 6a and 6b) suggesting enhanced mesoscale activity that is acting to flatten the isopycnals.

Briefly, 2D Leith with no SOP and 2D Leith as GM/Redi are discussed (Figures 9d and 9e). The primary response of GM in this case is to generate along isopycnal mixing. Without SOP, harm_2dleith_2.0_nSO has shallower denser waters ($\sigma_2 = 37$) in the south whereas harm_2dleith_2.0_gm has flatter isopycnals and deeper denser waters.

19422466, 2025, 9, Downloaded from https://agupubs.onlinelibrary.wiley.com/doi/10.1029/2025MS004950 by NICE, National Institute for Health and Care Excellence, Wiley Online Library on [16/12/2025]. See the Terms and Conditions (https://onlinelibrary.wiley.com/terms-and-conditions) on Wiley Online Library for rules of use; OA articles are governed by the applicable Creative Commons License

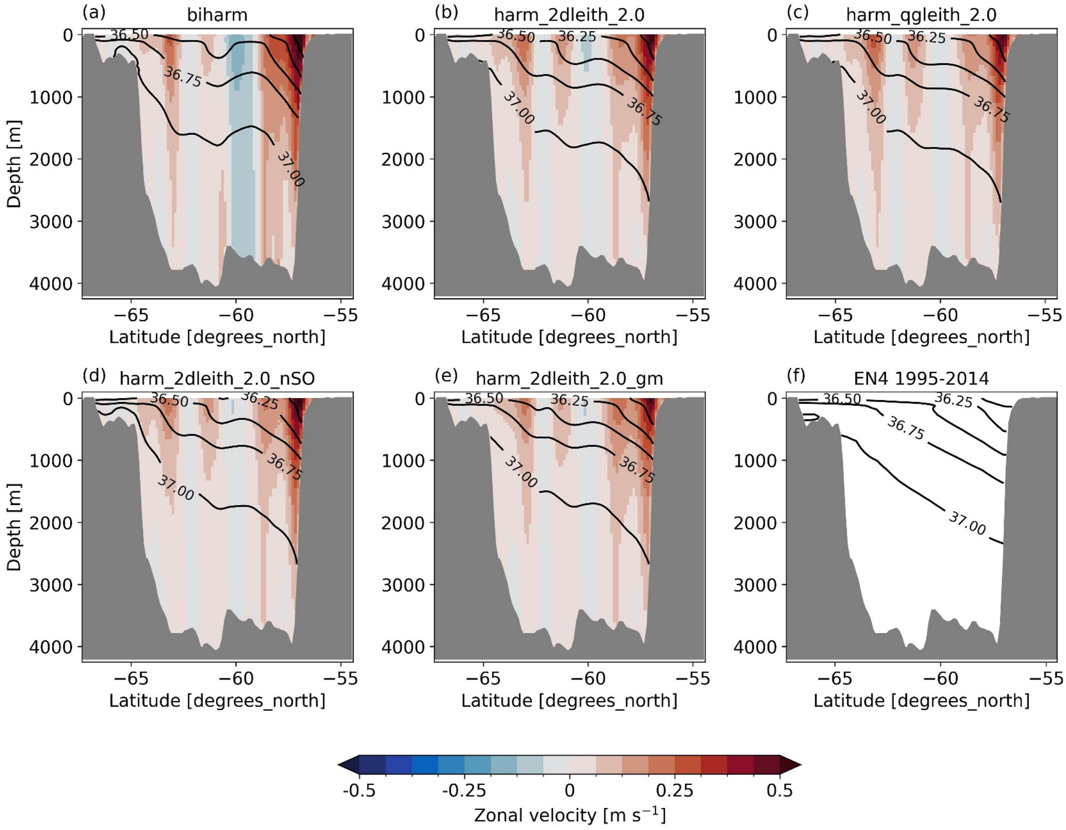

Figure 9. Zonal velocity through Drake Passage section 67°S–54°S, 292°E. Contour lines represent density referenced to 2,000 m, σ_2. In panel (a) biharm, (b) harm_2dleith_2.0, (c) harm_qgleith_2.0, (d) harm_2dleith_2.0_nSO, (e) harm_2dleith_2.0_gm, (f) σ_2 from EN4 2005–2014 time mean. Positive (negative) values represent eastward (westward) flow. Data is 1986–2009 time mean from second cycle.

5.2.2. Meridional Overturning

Figure 10 displays the zonally integrated overturning streamfunction in density coordinates across the latitude 80–30°S. Density is referenced to 2,000 m to capture overturning in the interior, which is not dissimilar to overturning on neutral density surfaces (Lee & Coward, 2003). The overturning streamfunction has been computed at each monthly model output and then averaged over the 1986 to 2009 period of the second cycle. The overarching picture from each simulation displays the key overturning cells in the SO, but we briefly describe the biharm simulation first (Figure 10a). Both the Lower and Subpolar Cells (densest water masses) have maximum transports over 10 Sv, with the Subpolar Cell highlighting the Antarctic gyres. The Upper Cell overturning with a transport of over 15 Sv is the main cell driven by the ACC, transforming deeper waters into intermediate waters. Finally, the Subtropical Cell are warmer lighter waters fed southwards that are downwelled into intermediate waters south of 40°S, which has a transport of ~17 Sv.

We now examine the SOP plus Leith viscosity simulations as all remaining simulations generally show the same pattern of response. Both harm_2dleith_2.0 and harm_qgleith_2.0 (Figures 10b and 10c) are consistent with the ACC timeseries (Figure 8). The increase in circumpolar transport is seen in the enhanced Upper Cell overturning, with an increase of ~2.5 Sv. The Leith schemes have reduced the Subtropical Cell by ~2.5 Sv. The increase in Upper Cell overturning and decrease in Subtropical Cell overturning implies there is more formation of Antarctic Intermediate Waters than Sub-Antarctic Mode Waters (SAMW). Both of these water masses are a key component of the MOC that enable the uptake of heat and carbon (Sabine et al., 2004). We will see how these changes to AAIW and SAMW formation have modified the temperature and salinity (Section 5.4). Moving on, the Subpolar gyres overturning is marginally weaker, though there does not appear to be a significant change in bottom water production with the introduction of the Leith schemes. In each case, the QG Leith scheme exhibits only a slightly greater response than the 2D Leith.

19422466, 2025, 9, Downloaded from https://agupubs.onlinelibrary.wiley.com/doi/10.1029/2025MS004950 by NICE, National Institute for Health and Care Excellence, Wiley Online Library on [16/12/2025]. See the Terms and Conditions (https://onlinelibrary.wiley.com/terms-and-conditions) on Wiley Online Library for rules of use; OA articles are governed by the applicable Creative Commons License

19422466, 2025, 9, Downloaded from https://agupubs.onlinelibrary.wiley.com/doi/10.1029/2025MS004950 by NICE, National Institute for Health and Care Excellence, Wiley Online Library on [16/12/2025]. See the Terms and Conditions (https://onlinelibrary.wiley.com/terms-and-conditions) on Wiley Online Library for rules of use; OA articles are governed by the applicable Creative Commons License

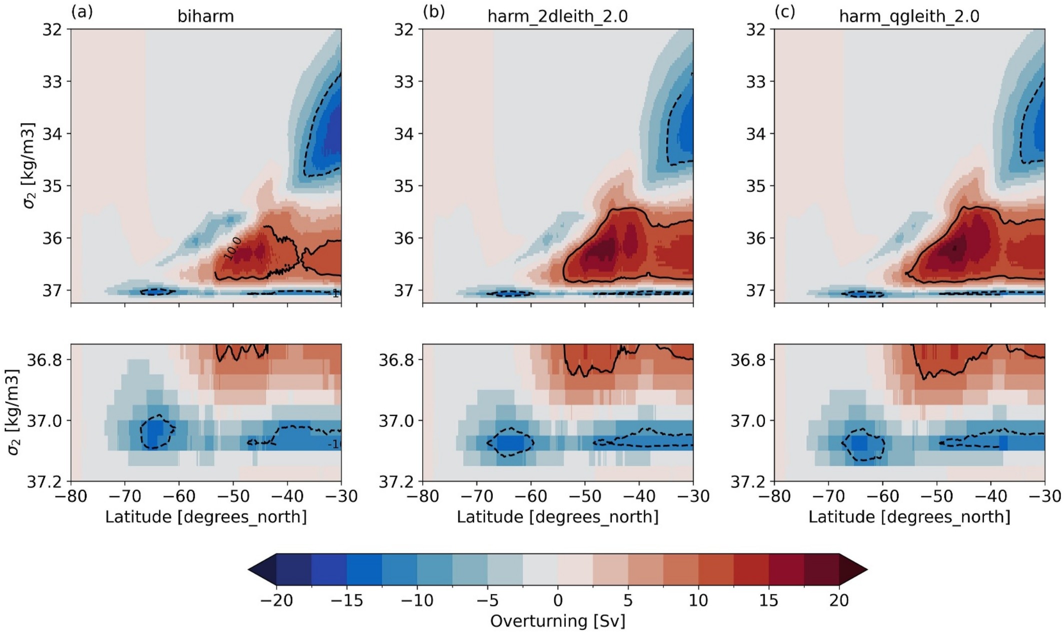

Figure 10. The time-mean Southern Ocean meridional overturning circulation (MOC) in density coordinates referenced to 2,000 m. In panel (a) standard biharmonic, (b) harmonic 2D Leith, (c) harmonic quasi-geostrophic Leith. The MOC is computed at each monthly model output and then time averaged over the 1986–2009 simulation period. Positive (negative) are clockwise (anticlockwise) circulation.

Contrasting the overturning strength with past studies and observations, the picture of the overturning in density coordinates presented in this work is similar to those given by Megann (2018) and Megann and Storkey (2021). Figure 6 in Megann and Storkey (2021) show how increased viscosity can modify the overturning cells, though the authors state that the overturning is only weakly sensitive to viscosity. Nevertheless, they show that increasing viscosity leads to a reduction in the Subtropical Cell and Lower Cell, along with an increase in the Upper Cell. We find similar results when we use the Leith schemes (Figure 10). Observational estimates of Lower Cell transport through 30°S lie in the range of 16–29 Sv (Lumpkin & Speer, 2007), showing that the Leith schemes have not improved this aspect. This could be related to how the NEMO model resolves across shelf slope processes (Storkey et al., 2025). Nevertheless, the too weak Lower Cell overturning is a feature of many CORE-II forced models (Farneti et al., 2015). Furthermore, the increased overturning transport of the Upper Cell is still within estimates of 15–21 Sv (Lumpkin & Speer, 2007) and the Leith simulations maintain the 12–18 Sv range in the Subtropical Cell (Ballarotta et al., 2013).

5.3. North Atlantic

5.3.1. Atlantic Meridional Overturning Circulation

The impact of the Leith schemes on the AMOC will now be discussed. This is in part because of the dynamical and thermodynamic connection between the SO and AMOC, as well as the AMOC's importance within the climate system (Buckley & Marshall, 2016). We also want to reiterate that the primary aim of this work is for the SO, the impact of the Leith schemes is global, notably seen through the AMOC.

Figure 11d shows a timeseries of maximum northward transport at 26°N. Over two cycles, all the simulations follow roughly the same troughs and peaks owing to the CORE-II forcing. In the first cycle, the strength of the AMOC in each simulation appears to be inversely related to the strength of the ACC (Figure 8), as could also be implied from Megann and Storkey (2021) Smagorinsky runs. For example, biharm and biharm_nSO have the largest AMOC, with peaks over 20 Sv, but have the weakest ACC transports of 120 and 110 Sv, respectively (Figure 8). The harm_qgleith runs have the weakest AMOC but the strongest ACC. In fact, this relationship has been attributed to the depth of the pycnocline (J. Marshall et al., 2017), where deepening will increase the ratio of ACC to AMOC transports, and shallowing vice versa. The inverse relationship is not the case for

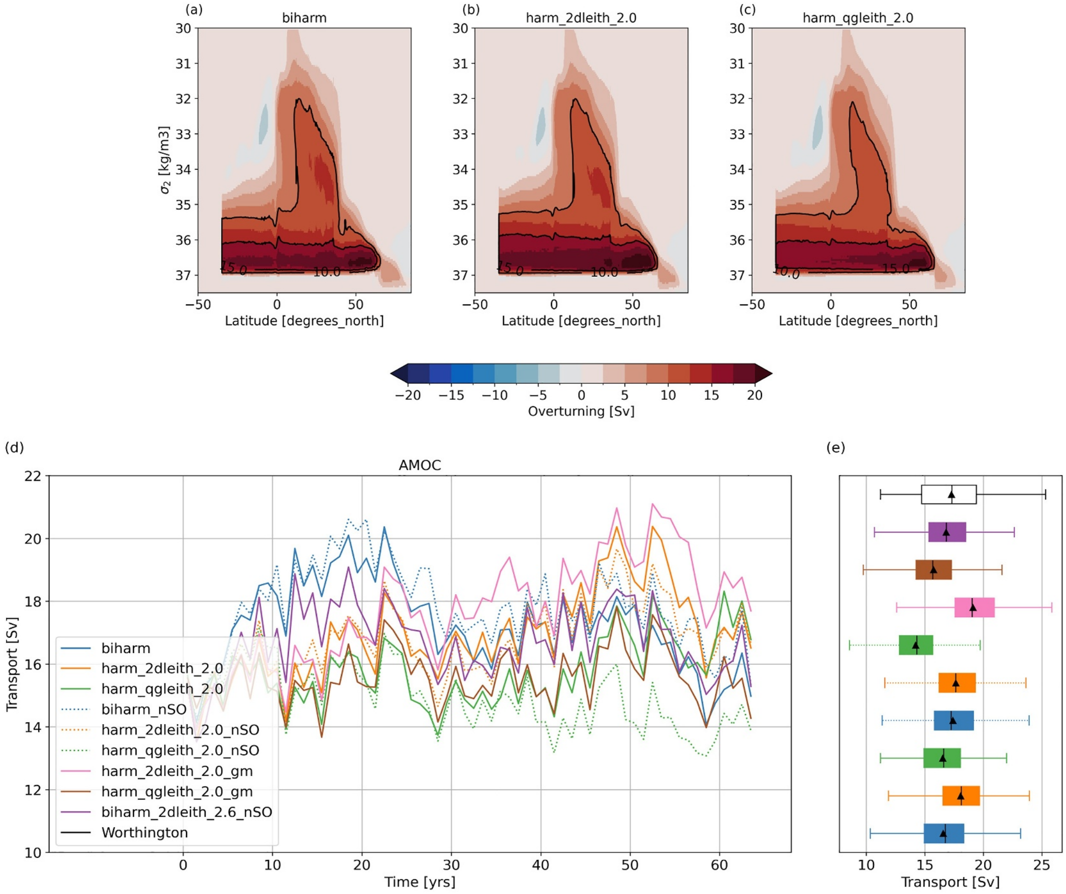

Figure 11. The Atlantic Meridional Overturning Circulation (AMOC). In panels (a–c) the AMOC in density coordinates referenced to 2,000 m computed over the Atlantic Basin, with (a) standard biharmonic, (b) harmonic 2D Leith, (c) harmonic quasi-geostrophic Leith. The data is computed at each monthly model output and then time averaged over the 1986–2009 simulation period in the second cycle. Positive (negative) are clockwise (anticlockwise) circulation. In panel (d) a time-series of the maximum northward transport of the AMOC at 26.5°N. The simulation data is computed for each monthly output and then yearly averaged. The bottom most line in the figure legend is the reconstruction by Worthington et al. (2021), which is yearly averaged. In panel (e) are box and whiskers, with mean (triangle) and median values (vertical line).

biharm_2dleith_2.6_nSO, which displays weaker AMOC and ACC transports, suggesting another mechanism may be at play. Nevertheless, most Leith runs remain within lower and upper observational limits, except QG Leith with no SOP and with GM/Redi (black box and whisker in Figure 11e).

In the second cycle, the inverse relation holds less strongly, likely relating to model drift (see Section 5.4). The 2D and QG Leith simulations begin to diverge, with the 2D Leith runs increasing their AMOC strength and the QG Leith runs maintaining their strength or becoming weaker. This divergence is seen in the Atlantic overturning in Figures 11b and 11c where harm_2dleith_2.0 shows an increase in northward transport across lighter waters. However, between years 40–50, harm_qgleith_2.0 is similar to biharm (Figure 11d), at least in the northward transport along the 15 Sv contour line, as shown in the overturning in Figures 11a–11c. The simulation with the weakest AMOC, harm_qgleith_2.0_nSO, in fact has the weakest Subtropical Cell overturning (not shown). However, the difference in Subtropical Cell overturning does not fully explain the difference between harm_2dleith_2.0 and harm_qgleith_2.0. Instead, the viscosity fields (Figure 6) provide some hints to explain the difference between 2D and QG Leith. Within subpolar regions, greater mixing in QG Leith could be modifying the stratification required for a stronger AMOC. Indeed, we see higher viscosity along the boundary currents, dampening mesoscale eddies, which promote interior subpolar gyre deep water formation (Johnson et al., 2019; Tagklis et al., 2020).

19422466, 2025, 9, Downloaded from https://agupubs.onlinelibrary.wiley.com/doi/10.1029/2025MS004950 by NICE, National Institute for Health and Care Excellence, Wiley Online Library on [16/12/2025]. See the Terms and Conditions (https://onlinelibrary.wiley.com/terms-and-conditions) on Wiley Online Library for rules of use; OA articles are governed by the applicable Creative Commons License

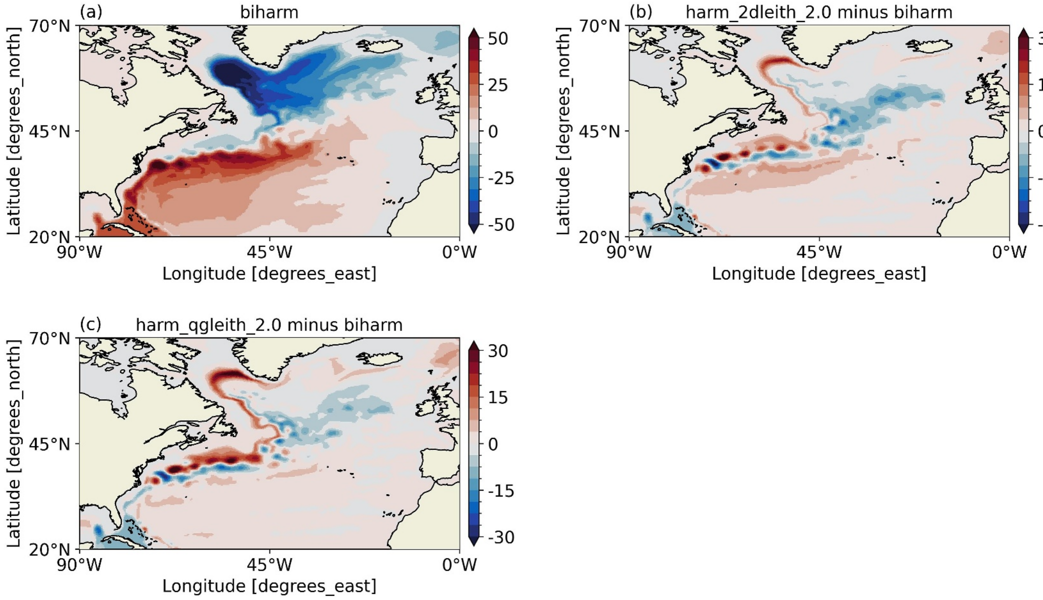

Figure 12. Barotropic stream function computed using the zonal and vertical integral of meridional velocity. In panel (a) biharm, (b) harm_2dleith_2.0 minus biharm, (c) harm_qgleith_2.0 minus biharm. Data computed at monthly intervals and averaged over second cycle in 1986–2009 period.

5.3.2. Barotropic Stream Function

To conclude this section on the NA, we present the barotropic stream function for the reference (biharm) and then the anomaly (Leith minus reference) for harm_2dleith_2.0 and harm_qgleith_2.0 in Figure 12. By plotting the stream function we can better understand some of the circulation and transport changes in this region. The biharm simulation displays the anticlockwise sub polar gyre (blue shading) and the clockwise sub tropical gyre (red shading). Transport in the Florida Strait reaches a maximum of around 40 Sv, greater than observations of just over 30 Sv (Worthington et al., 2021). The Labrador Sea (LS) transport is upwards of 50 Sv at its maximum, close to previous estimates (Reynaud et al., 1995).

Now we look at the anomalies. The change in transport is generally consistent with the viscosity spatial pattern and values (Figures 6b and 6c). The stream function response to 2D Leith (Figure 12b) is for the western subpolar gyre and GS to weaken. However, the eastern subpolar gyre and south of the GS both strengthen. The increase in transport in the subtropical gyre likely explains harm_2dleith_2.0 increase in AMOC (Figure 11e). QG Leith viscosity is greater through the GS region and surrounding the LS, and here we see the greatest changes in transport—a maximum of 30 Sv reduction in the LS and north of the GS (Figure 12c). Despite the transport differences, biharm and harm_qgleith_2.0 have similar AMOC strength (Figure 11), which we only examine at 26°N. It is clear that changes are being made to the circulation in the GS and LS in response to changes in viscosity and mesoscale eddy dissipation.

5.4. Model Drift and Biases

We begin the final results section by examining global model drifts in temperature and salinity (Figure 13) for three simulations: biharm; harm_2dleith_2.0; and harm_qgleith_2.0. Much work has gone in to reducing model drifts in Global Ocean configurations over a 30 year spin up cycle (Guiavarc'h et al., 2025; Megann & Storkey, 2021; Megann et al., 2014). Here we show the drift over the full 64 years. The biharm simulation has around 0.16°C of warming at the surface and up to −0.16°C of cooling below 200 m (Figure 13a). There is a freshening of −0.06 g/kg centered at 300 m depth, and below 600 m salinity increases initially but remains stable (Figure 13b). In the two Leith runs, the temperature drifts exhibit a strong subsurface warming of $0.3 - 0.4$°C at 64 years, with the strongest response in harm_qgleith_2.0 (Figures 13c–13e). At the surface there is a slight decrease in warming compared to biharm, but the trend is stable. The salinity drifts are not too dissimilar from biharm, showing an increase in salinity below 200 m, associated with the warming. The difference in model drift

19422466, 2025, 9, Downloaded from https://agupubs.onlinelibrary.wiley.com/doi/10.1029/2025MS004950 by NICE, National Institute for Health and Care Excellence, Wiley Online Library on [16/12/2025]. See the Terms and Conditions (https://onlinelibrary.wiley.com/terms-and-conditions) on Wiley Online Library for rules of use; OA articles are governed by the applicable Creative Commons License

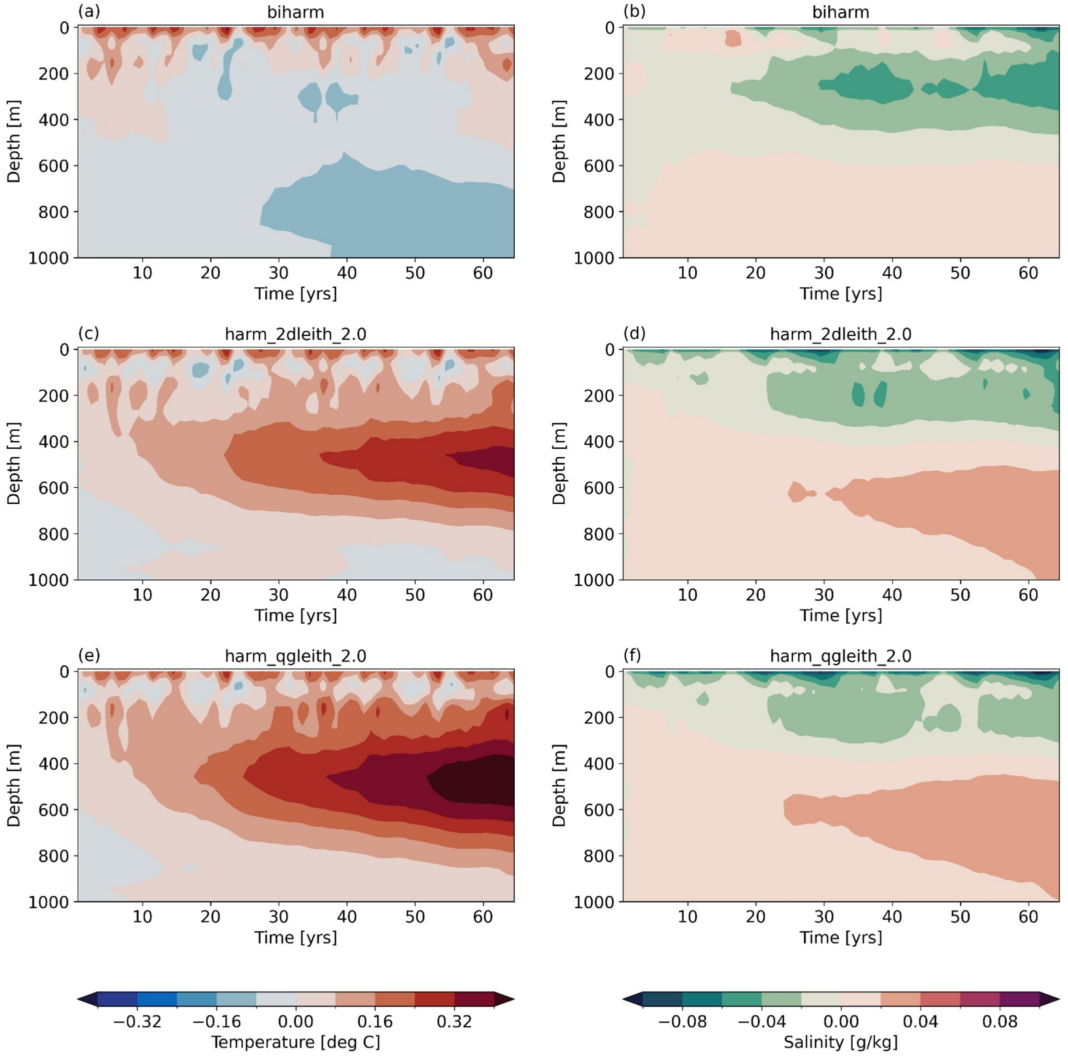

Figure 13. Temperature (left panels) and salinity (right panels) drift computed using yearly means over complete 64 year simulation period. In panels (a, b) biharm, (c, d) harm_2dleith_2.0, (e, f) harm_qgleith_2.0.

between 2D and QG Leith is small, suggesting localized changes may be at play that explain the divergence in AMOC in the second cycle (Figure 11d).

Moving on, we present global fields of biases and simulation differences. These are shown at a depth of 300 m in Figure 14. The bias shows the difference between the reference simulation and EN4 climatology and the differences are those between the Leith runs and biharm. The temperature bias has a similar profile to Figure 9a in Guiavarc'h et al. (2025), who look at potential temperature at 100 m depth. However, due to the additional cycle, period of averaging, and difference in depth, we see an amplification of these biases, notably across the NA, Kuroshio, and SO.

In the Leith runs (Figures 14c–14e), there is a strong warming throughout the Atlantic, and a cooling surrounding the Antarctic coastline. The warming helps to reduce some of the Atlantic cool bias in the subtropical gyre and the cooling reduces the warm bias around Antarctica. North of the ACC belt exhibits warming in response to the enhanced ACC transport (Figure 8) and Upper Cell overturning (Figure 10). Interestingly, this pattern of strong warming north of the ACC is not shown in Megann and Storkey (2021) Figure 10, perhaps owing to the difference in actions of the harmonic and biharmonic operators on the large-scale flow. In the NA, the GS cool bias and eastern subpolar gyre warm bias are both reduced. However, the large cool bias is still present. These biases are still related to the misrepresentation of the GS and NA Current pathways in ORCA025 (Guiavarc'h et al., 2025).

19422466, 2025, 9, Downloaded from https://agupubs.onlinelibrary.wiley.com/doi/10.1029/2025MS004950 by NICE, National Institute for Health and Care Excellence, Wiley Online Library on [16/12/2025]. See the Terms and Conditions (https://onlinelibrary.wiley.com/terms-and-conditions) on Wiley Online Library for rules of use; OA articles are governed by the applicable Creative Commons License

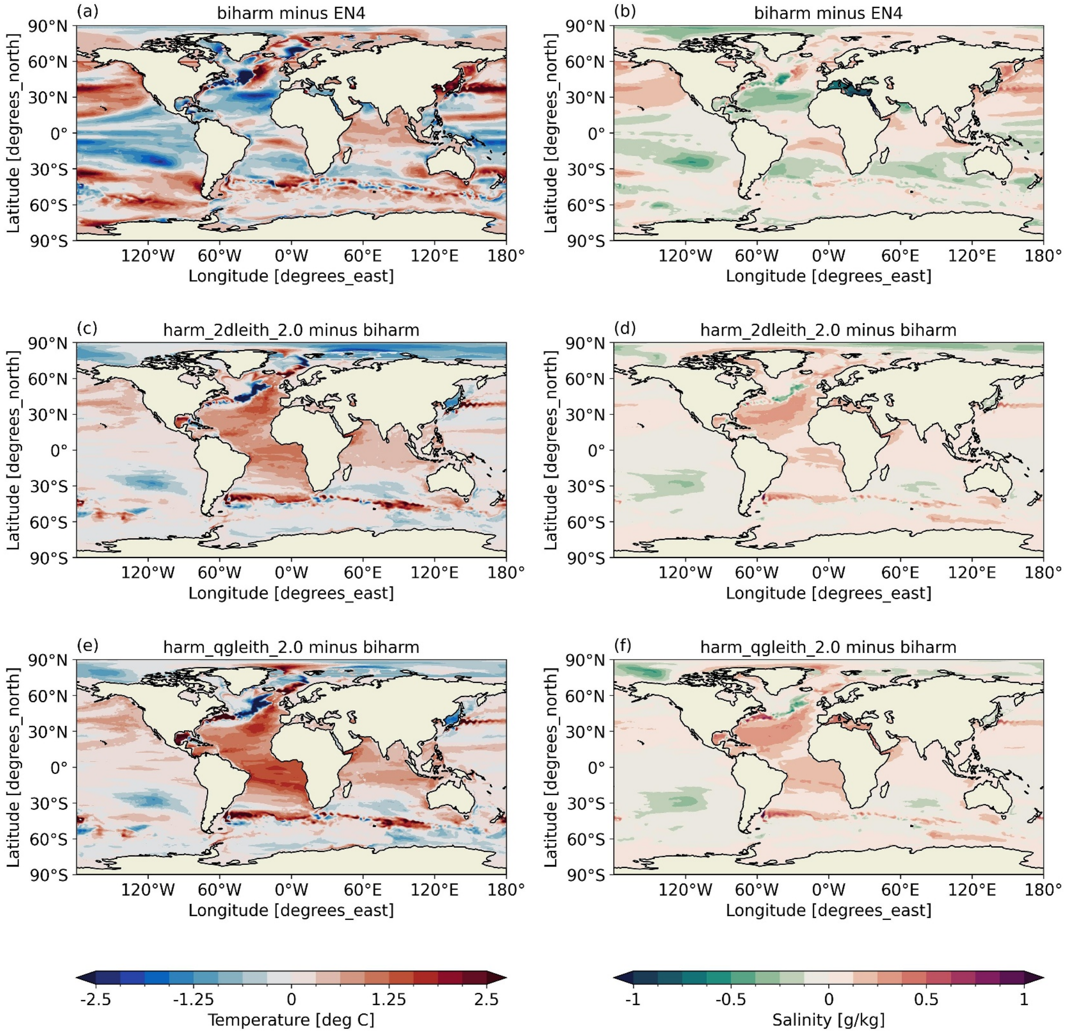

Figure 14. Temperature (left) and salinity (right) at 300 m. In panels (a, b) biharm minus EN4, and (c, d) harm_2dleith_2.0, and (e, f) harm_qgleith_2.0. Model data is averaged over the 1986–2009 period in the second cycle, and EN4 climatology (Good et al., 2013) averaged over the 1995–2014 period.

Further, the change in biases are consistent with the barotropic stream function transport, where a cooling in the eastern subpolar gyre is in response to a stronger cyclonic gyre and upwelling of cooler waters from depth. Compared to harm_qgleith_2.0, harm_2dleith_2.0 shows a stronger warming along the boundary currents of the Irminger and Labrador seas. The NA cooling in harm_qgleith_2.0 stretches north east, perhaps preventing the inflow of warmer, and saline (Figures 14d–14f), waters into this region via the Irminger Current, which is necessary for deep water formation in the subpolar gyres (Rhein et al., 2011). Using Leith as GM/Redi results in greater warming and degradation of the NA subpolar gyre (not shown), an issue similarly encountered in Storkey et al. (2025) when κ_{gm} is capped with a value larger than 75 $m^2\ s^{-1}$.

Our focus now turns to briefly discussing mechanisms associated with changes in model drift and global temperature fields. Megann and Storkey (2021) show a gradual reduction in subsurface cooling with an increase in viscosity. This reduction in cooling also coincides with an increase in ACC transport (~ 10%), though not to the extent we show here (Figure 8). In this work, the increase in both ACC transport and overturning of the SO Upper Cell provide a pathway for additional heat and salinity to penetrate from the surface to intermediate depths, as suggested by the temperature fields in Figure 14. Moreover, harm_qgleith_2.0 has greater viscosity than harm_2dleith_2.0 in the upper ocean (Figure 7a), so we can expect greater mesoscale eddy dissipation. This implies enhanced northward Ekman transport of heat and greater model drift in harm_qgleith_2.0, as shown in

19422466, 2025, 9, Downloaded from https://agupubs.onlinelibrary.wiley.com/doi/10.1029/2025MS004950 by NICE, National Institute for Health and Care Excellence, Wiley Online Library on [16/12/2025]. See the Terms and Conditions (https://onlinelibrary.wiley.com/terms-and-conditions) on Wiley Online Library for rules of use; OA articles are governed by the applicable Creative Commons License

Figures 13 and 14. In addition, the warming Atlantic subtropical gyres could be in response to a deeper pycnocline due to increased eddy dissipation (Mak et al., 2022). Despite harm_qgleith_2.0 having greater warming and seemingly increased heat capacity north of the ACC and Atlantic, this does not correspond to any significant changes in the AMOC strength at 26°N (Figure 11d). This change is attributed to the increased viscosity—of QG Leith against 2D Leith—and implied dissipation of eddies in the NA, where eddies make important contributions to the northwards transport of heat and mass (Zhai & Yang, 2022).

6. Summary and Discussion

In this work we have implemented the 2D and QG Leith subgrid scale- and flow-aware eddy closures in NEMO v4.0.4. We have explored the utility of theses schemes in an eddy-resolving idealized channel model and a realistic eddy-permitting forced global model, GOSI9 ORCA025. A detailed exploration of the terms that make up the QG Leith viscosity coefficient was examined in the channel model, effectively highlighting the inhomogeneity of the stretching and vorticity contributions. A small ensemble of nine ORCA025 simulations were then completed, where the Leith schemes were employed as the viscosity coefficient, with harmonic variants used as eddy and tracer diffusion. Results from the global simulations show the Leith schemes can modulate key circulation features, such as the ACC and AMOC.

Across the idealized and realistic model results, the ocean demonstrates a modest response to the Leith subgrid closures under forced atmospheric conditions. It is clear that the Leith schemes do improve some of the poor metrics identified in analyses conducted from CMIP6 (Beadling et al., 2020; Kuhlbrodt et al., 2018; Roberts et al., 2019). Both Leith runs with the SOP show increased ACC transports and similar maximum AMOC transports—difference of 1–2 Sv. The difference between 2D and QG Leith is the stretching term and this adds further mesoscale eddy dissipation to regions that are in the QG regime. In the case of QG Leith with SOP, the ACC transport is one of the strongest and the AMOC is similar to the reference GOSI9 simulation in the second cycle. Some improvements are made to model biases, in particular the cooling of the warm bias surrounding Antarctica and reduction of biases in the Atlantic subtropics, GS, and east of the NA subpolar gyre. Without SOP and with Leith as GM/Redi, the simulations show either little sensitivity, little difference, or display a weakened AMOC, in the case of QG Leith no SOP. As a result, we propose the QG Leith viscosity scheme should be considered as a viable alternative to the biharmonic grid-aware scheme used in the GOSI9 configuration. Moreover, it is theoretically more suitable for the eddy-permitting regime than the current biharmonic and Smagorinsky schemes in NEMO.

Our recommendation of the QG Leith viscosity scheme comes with caution. In this work we have ensured the Leith viscosity schemes are working as intended by exploring their implementation in the idealized model. The global model is then used to test how the schemes influence the SO circulation and the NA. However, the Leith schemes have been immediately tested in the same parameter space devised by the Joint Marine Modeling Program for GOSI9. It is important to consider the incremental nature of model development, with any change receiving a thorough exploration of the parameter space, before decisions are made for their use in future model configurations. So the recommendation made here may change once further investigations are made on the appropriate parameter space. Our initial challenge with these schemes was grid-scale noise, which we alleviated by increasing Λ. This may be a result of these schemes producing too high levels of grid-scale energy in eddy-permitting models (Bachman et al., 2017), though further parameter tuning could help here. For example, the vector-invariant momentum advection on non-uniform mesh grids leads to noise in the vertical velocity field (Danilov & Wang, 2015), with the Hollingsworth et al. (1983) formulation reducing the grid-scale noise. Since the Leith schemes depend on the divergence fields, it may mean some minor tuning of the Hollingsworth formulation is required, which may enable Λ to be reduced. In addition, consideration should be placed on the accuracy of tracer and advection schemes since these can modulate the energy cascade (Soufflet et al., 2016).

The discussion so far has focused on the utility of the QG Leith harmonic viscosity scheme over the current biharmonic grid-aware scheme. Although the Smagorinsky-like biharmonic scheme (Griffies & Hallberg, 2000) is theoretically ill-suited to the eddy-permitting regime, it is still necessary to discuss its application in these classes of model. Megann and Storkey (2021) explored biharmonic Smagorinsky by increasing the scaling parameter C, from 2 to 4 (see Equation 4). As C was increased, resulting improvements were reported in the Atlantic cool bias and the cool subsurface model drift, primarily as a result of reduced numerical mixing. However, there were little changes in the SO, notably no real increase in ACC transport when using $C = 4$,

19422466, 2025, 9, Downloaded from https://agupubs.onlinelibrary.wiley.com/doi/10.1029/2025MS004950 by NICE, National Institute for Health and Care Excellence, Wiley Online Library on [16/12/2025]. See the Terms and Conditions (https://onlinelibrary.wiley.com/terms-and-conditions) on Wiley Online Library for rules of use; OA articles are governed by the applicable Creative Commons License

producing no noticeable improvement in SO biases. This is contrasted with Leith, which does lead to improvements here. With the recent development of GOSI9, it would be interesting to make a direct comparison of Leith with the Smagorinsky-like biharmonic scheme in the same model configuration.

The basis of this study set out to utilize a scheme that could offer a complete solution to the stubborn issues present in NEMO ORCA025, notably the Global Ocean configurations. In some regimes, the Leith subgrid closures can represent viscosity, and eddy and tracer diffusivity. However, through the vertical profiles of viscosity, these did not match observations found in Groeskamp et al. (2020), particularly in the SO. This forms part of our decision to propose only using the QG Leith viscosity at present with the SOP. The SOP has been carefully developed and is fully tested, so replacing only the viscosity coefficient with QG Leith presently does seem prudent. In spite of this, we do propose further testing of Leith plus GM (not Redi) in ORCA025 as it remains under explored and is currently one of the only viable solutions to the GM parameterization in eddy-permitting ocean models.

In this study we have only touched the surface, leaving room for more in-depth and detailed studies. Recent work has investigated resolution dependency on overturning in the subpolar NA (Petit et al., 2023) and the AMOC coherence between the OSNAP arrays and the midlatitudes (Petit et al., 2025). It would be interesting to explore how sensitive these studies are to the viscosity parameterization used, notably after tuning the ocean model for the Leith schemes. Another aspect worth studying is the energetics, as has been done previously across ORCA resolutions (Kjellsson & Zanna, 2017). Exploring the cascade with a focus on the SO may provide further clues into why the ACC transport is weak in GOSI9. Furthermore, it is currently unclear how the Leith schemes would perform under a coupled atmosphere in HadGEM3-GC3.1, though findings from Storkey et al. (2025) suggest we may see similar continued improvements in ACC transport. However, in this study we have employed NEMO v4.0.4. Any future studies should be made with more recent NEMO releases, where GOSI10 uses v4.2.x and GOSI11 is being developed with v5.x. Ongoing effort is underway to implement the Leith viscosity schemes into the NEMO v5.x trunk.

Data Availability Statement

The NEMO model is freely available from the NEMO website (https://www.nemo-ocean.eu/, last access: 9 January 2025). The source code used in these experiments, including namelist and modified Fortran routines, are located at Wilder (2025b). The data to reproduce the figures in this paper are located at Wilder (2025c). The scripts to analyze and plot the figures are located at Wilder (2025a). The CDFTOOLS Fortran 90 package (https://github.com/meom-group/CDFTOOLS, last access: 9 January 2025) is available on GitHub under the CeCILL license (http://www.cecill.info/licences/Licence_CeCILL_V2-en.html) and was used to run part of the analysis. The AMOC reconstruction data of Worthington et al. (2021) is found at Worthington et al. (2022).

Acknowledgments

This work was funded by the European Union's Horizon 2020 research and innovation programme under grant agreement no. 101003536 (ESM2025—Earth System Models for the Future). The work was also partially supported by the European Union's Horizon Europe research and innovation programme under grant agreement no. 101137682 (AI4PEX - Artificial Intelligence and Machine Learning for Enhanced Representation of Processes and Extremes in Earth System Models). The analysis was performed on JASMIN (http://jasmin.ac.uk/), the UK collaborative data analysis facility. Simulations were performed on Monsoon2, a collaborative High-Performance Computing facility funded by the Met Office and the Natural Environment Research Council. We would like to thank the anonymous reviewers for their comments and suggestions, leading to a much improved manuscript. The authors would also like to thank Robin Smith and Remi Tailleux for their constructive comments on this manuscript.

References

Abernathey, R., Cerovecki, I., Holland, P. R., Newsom, E., Mazloff, M., & Talley, L. D. (2016). Water-mass transformation by sea ice in the upper branch of the Southern Ocean overturning. *Nature Geoscience*, *9*(8), 596–601. https://doi.org/10.1038/ngeo2749

Abernathey, R., Marshall, J., & Ferreira, D. (2011). The dependence of Southern Ocean meridional overturning on wind stress. *Journal of Physical Oceanography*, *41*(12), 2261–2278. https://doi.org/10.1175/JPO-D-11-023.1

Abernathey, R., Marshall, J., Mazloff, M., & Shuckburgh, E. (2010). Enhancement of mesoscale eddy stirring at steering levels in the Southern Ocean. *Journal of Physical Oceanography*, *40*(1), 170–184. https://doi.org/10.1175/2009JPO4201.1

Adcroft, A., Anderson, W., Balaji, V., Blanton, C., Bushuk, M., Dufour, C. O., et al. (2019). The GFDL Global Ocean and sea ice model OM4.0: Model description and simulation features. *Journal of Advances in Modeling Earth Systems*, *11*(10), 3167–3211. https://doi.org/10.1029/2019MS001726

Bachman, S. D. (2019). The GM+E closure: A framework for coupling backscatter with the Gent and McWilliams parameterization. *Ocean Modelling*, *136*, 85–106. https://doi.org/10.1016/j.ocemod.2019.02.006

Bachman, S. D., Fox-Kemper, B., & Pearson, B. (2017). A scale-aware subgrid model for quasi-geostrophic turbulence. *Journal of Geophysical Research: Oceans*, *122*(2), 1529–1554. https://doi.org/10.1002/2016JC012265

Ballarotta, M., Drijfhout, S., Kuhlbrodt, T., & Döös, K. (2013). The residual circulation of the Southern Ocean: Which spatio-temporal scales are needed? *Ocean Modelling*, *64*, 46–55. https://doi.org/10.1016/j.ocemod.2013.01.005

Beadling, R. L., Russell, J. L., Stouffer, R. J., Mazloff, M., Talley, L. D., Goodman, P. J., et al. (2020). Representation of Southern Ocean properties across coupled model intercomparison project generations: CMIP3 to CMIP6. *Journal of Climate*, *33*(15), 6555–6581. https://doi.org/10.1175/JCLI-D-19-0970.1

Blockley, E., Fiedler, E., Ridley, J., Roberts, L., West, A., Copsey, D., et al. (2023). The sea ice component of GC5: Coupling SI^3 to HadGEM3 using conductive fluxes. *EGUsphere*, 1–27. https://doi.org/10.5194/egusphere-2023-1731

Boucher, O., Servonnat, J., Albright, A. L., Aumont, O., Balkanski, Y., Bastrikov, V., et al. (2020). Presentation and evaluation of the IPSL-CM6A-LR climate model. *Journal of Advances in Modeling Earth Systems*, *12*(7), e2019MS002010. https://doi.org/10.1029/2019MS002010

Buckley, M. W., & Marshall, J. (2016). Observations, inferences, and mechanisms of the Atlantic meridional overturning circulation: A review. *Reviews of Geophysics*, *54*(1), 5–63. https://doi.org/10.1002/2015RG000493

19422466, 2025, 9, Downloaded from https://agupubs.onlinelibrary.wiley.com/doi/10.1029/2025MS004950 by NICE, National Institute for Health and Care Excellence, Wiley Online Library on [16/12/2025]. See the Terms and Conditions (https://onlinelibrary.wiley.com/terms-and-conditions) on Wiley Online Library for rules of use; OA articles are governed by the applicable Creative Commons License

Bullister, J. L., Rhein, M., & Mauritzen, C. (2013). Chapter 10—Deepwater formation. In G. Siedler, S. M. Griffies, J. Gould, & J. A. Church (Eds.), *International geophysics* (Vol. 103, pp. 227–253). Academic Press. https://doi.org/10.1016/B978-0-12-391851-2.00010-6

Calvin, K., Dasgupta, D., Krinner, G., Mukherji, A., Thorne, P. W., Trisos, C., et al. (2023). IPCC, 2023: Climate change 2023: Synthesis report. In H. Lee & J. Romero (Eds.), *Contribution of working groups I, II and III to the sixth assessment report of the intergovernmental panel on climate change [core writing team] (technical report)* (1st ed.). Intergovernmental Panel on Climate Change (IPCC). https://doi.org/10.59327/IPCC/AR6-9789291691647

Charney, J. G. (1971). Geostrophic turbulence. *Journal of Atmospheric Sciences*, *28*(6), 1087–1095. https://doi.org/10.1175/1520-0469(1971)028⟨1087:GT⟩2.0.CO;2

Chelton, D. B., de Szoeke, R. A., Schlax, M. G., Naggar, K. E., & Siwertz, N. (1998). Geographical variability of the first baroclinic Rossby radius of deformation. *Journal of Physical Oceanography*, *28*(3), 433–460. https://doi.org/10.1175/1520-0485(1998)028⟨0433:GVOTFB⟩2.0.CO;2

Couto, N., Martinson, D. G., Kohut, J., & Schofield, O. (2017). Distribution of upper circumpolar deep water on the warming continental shelf of the West Antarctic Peninsula. *Journal of Geophysical Research: Oceans*, *122*(7), 5306–5315. https://doi.org/10.1002/2017JC012840

Cunningham, S. A., Alderson, S. G., King, B. A., & Brandon, M. A. (2003). Transport and variability of the Antarctic circumpolar current in Drake passage. *Journal of Geophysical Research*, *108*(C5), 8084. https://doi.org/10.1029/2001JC001147

Danilov, S., & Wang, Q. (2015). Resolving eddies by local mesh refinement. *Ocean Modelling*, *93*, 75–83. https://doi.org/10.1016/j.ocemod.2015.07.006

Donohue, K. A., Tracey, K. L., Watts, D. R., Chidichimo, M. P., & Chereskin, T. K. (2016). Mean Antarctic circumpolar current transport measured in Drake passage. *Geophysical Research Letters*, *43*(22), 11760–11767. https://doi.org/10.1002/2016GL070319

Downes, S., Spence, P., & Hogg, A. (2018). Understanding variability of the Southern Ocean overturning circulation in CORE-II models. *Ocean Modelling*, *123*, 98–109. https://doi.org/10.1016/j.ocemod.2018.01.005

Evans, D. G., Holliday, N. P., Bacon, S., & Le Bras, I. (2023). Mixing and air–sea buoyancy fluxes set the time-mean overturning circulation in the subpolar North Atlantic and Nordic Seas. *Ocean Science*, *19*(3), 745–768. https://doi.org/10.5194/os-19-745-2023

Farneti, R., Downes, S. M., Griffies, S. M., Marsland, S. J., Behrens, E., Bentsen, M., et al. (2015). An assessment of Antarctic Circumpolar Current and Southern Ocean meridional overturning circulation during 1958–2007 in a suite of interannual CORE-II simulations. *Ocean Modelling*, *93*, 84–120. https://doi.org/10.1016/j.ocemod.2015.07.009

Ferreira, D., Marshall, J., & Heimbach, P. (2005). Estimating eddy stresses by fitting dynamics to observations using a residual-mean ocean circulation model and its adjoint. *Journal of Physical Oceanography*, *35*(10), 1891–1910. https://doi.org/10.1175/JPO2785.1

Fox-Kemper, B., Adcroft, A., Böning, C. W., Chassignet, E. P., Curchitser, E., Danabasoglu, G., et al. (2019). Challenges and prospects in ocean circulation models. *Frontiers in Marine Science*, *6*, 65. https://doi.org/10.3389/fmars.2019.00065

Fox-Kemper, B., & Menemenlis, D. (2008). Can large eddy simulation techniques improve mesoscale rich ocean models? In *Ocean modeling in an eddying regime* (pp. 319–337). https://doi.org/10.1029/177GM19

Frölicher, T. L., Sarmiento, J. L., Paynter, D. J., Dunne, J. P., Krasting, J. P., & Winton, M. (2015). Dominance of the Southern Ocean in anthropogenic carbon and heat uptake in CMIP5 models. *Journal of Climate*, *28*(2), 862–886. https://doi.org/10.1175/JCLI-D-14-00117.1

Gaspar, P., Grégoris, Y., & Lefevre, J.-M. (1990). A simple eddy kinetic energy model for simulations of the oceanic vertical mixing: Tests at station Papa and long-term upper ocean study site. *Journal of Geophysical Research*, *95*(C9), 16179–16193. https://doi.org/10.1029/JC095iC09p16179

Gent, P. R., & McWilliams, J. C. (1990). Isopycnal mixing in Ocean Circulation models. *Journal of Physical Oceanography*, *20*(1), 150–155. https://doi.org/10.1175/1520-0485(1990)020⟨0150:IMIOCM⟩2.0.CO;2

Gent, P. R., Willebrand, J., McDougall, T. J., & McWilliams, J. C. (1995). Parameterizing eddy-induced tracer transports in ocean circulation models. *Journal of Physical Oceanography*, *25*(4), 463–474. https://doi.org/10.1175/1520-0485(1995)025⟨0463:PEITTI⟩2.0.CO;2

Gill, A. E. (1982). *Atmosphere-ocean dynamics*. Academic Press.

Gille, S. T. (1997). The Southern Ocean momentum balance: Evidence for topographic effects from numerical model output and altimeter data. *Journal of Physical Oceanography*, *27*(10), 2219–2232. https://doi.org/10.1175/1520-0485(1997)027⟨2219:TSOMBE⟩2.0.CO;2

Gille, S. T. (2003). Float observations of the Southern Ocean. Part II: Eddy fluxes. *Journal of Physical Oceanography*, *33*(6), 1182–1196. https://doi.org/10.1175/1520-0485(2003)033⟨1182:FOOTSO⟩2.0.CO;2

Good, S. A., Martin, M. J., & Rayner, N. A. (2013). EN4: Quality controlled ocean temperature and salinity profiles and monthly objective analyses with uncertainty estimates. *Journal of Geophysical Research: Oceans*, *118*(12), 6704–6716. https://doi.org/10.1002/2013JC009067

Griffies, S. M. (2004). *Fundamentals of ocean climate models*. Princeton University Press. https://doi.org/10.2307/j.ctv301gzg

Griffies, S. M., & Hallberg, R. W. (2000). Biharmonic friction with a Smagorinsky-like viscosity for use in large-scale eddy-permitting ocean models. *Monthly Weather Review*, *128*(8), 2935–2946. https://doi.org/10.1175/1520-0493(2000)128⟨2935:BFWASL⟩2.0.CO;2

Groeskamp, S., LaCasce, J. H., McDougall, T. J., & Rogé, M. (2020). Full-depth global estimates of ocean mesoscale eddy mixing from observations and theory. *Geophysical Research Letters*, *47*(18), e2020GL089425. https://doi.org/10.1029/2020GL089425

Grooms, I. (2023). Backscatter in energetically-constrained Leith parameterizations. *Ocean Modelling*, *186*, 102265. https://doi.org/10.1016/j.ocemod.2023.102265

Guiavarc'h, C., Storkey, D., Blaker, A. T., Blockley, E., Megann, A., Hewitt, H., et al. (2025). GOSI9: UK Global Ocean and Sea Ice configurations. *Geoscientific Model Development*, *18*(2), 377–403. https://doi.org/10.5194/gmd-18-377-2025

Hallberg, R. (2013). Using a resolution function to regulate parameterizations of oceanic mesoscale eddy effects. *Ocean Modelling*, *72*, 92–103. https://doi.org/10.1016/j.ocemod.2013.08.007

Hewitt, H. T., Roberts, M., Mathiot, P., Biastoch, A., Blockley, E., Chassignet, E. P., et al. (2020). Resolving and parameterising the ocean mesoscale in earth system models. *Current Climate Change Reports*, *6*(4), 137–152. https://doi.org/10.1007/s40641-020-00164-w

Hollingsworth, A., Kållberg, P., Renner, V., & Burridge, D. M. (1983). An internal symmetric computational instability. *Quarterly Journal of the Royal Meteorological Society*, *109*(460), 417–428. https://doi.org/10.1002/qj.49710946012

Holte, J., Talley, L. D., Gilson, J., & Roemmich, D. (2017). An Argo mixed layer climatology and database. *Geophysical Research Letters*, *44*(11), 5618–5626. https://doi.org/10.1002/2017GL073426

Ilıcak, M. (2016). Quantifying spatial distribution of spurious mixing in ocean models. *Ocean Modelling*, *108*, 30–38. https://doi.org/10.1016/j.ocemod.2016.11.002

Johnson, H. L., Cessi, P., Marshall, D., Schloesser, F., & Spall, M. A. (2019). Recent contributions of theory to our understanding of the Atlantic meridional overturning circulation. *Journal of Geophysical Research: Oceans*, *124*(8), 5376–5399. https://doi.org/10.1029/2019JC015330

Kjellsson, J., & Zanna, L. (2017). The impact of horizontal resolution on energy transfers in global ocean models. *Fluids*, *2*(3), 45. https://doi.org/10.3390/fluids2030045

Klocker, A., & Abernathey, R. (2014). Global patterns of mesoscale eddy properties and diffusivities. *Journal of Physical Oceanography*, *44*(3), 1030–1046. https://doi.org/10.1175/JPO-D-13-0159.1

19422466, 2025, 9, Downloaded from https://agupubs.onlinelibrary.wiley.com/doi/10.1029/2025MS004950 by NICE, National Institute for Health and Care Excellence, Wiley Online Library on [16/12/2025]. See the Terms and Conditions (https://onlinelibrary.wiley.com/terms-and-conditions) on Wiley Online Library for rules of use; OA articles are governed by the applicable Creative Commons License

Koenig, Z., Provost, C., Ferrari, R., Sennéchael, N., & Rio, M.-H. (2014). Volume transport of the Antarctic Circumpolar Current: Production and validation of a 20 year long time series obtained from in situ and satellite observations. *Journal of Geophysical Research: Oceans*, *119*(8), 5407–5433. https://doi.org/10.1002/2014JC009966

Kolmogorov, A. N. (1941). The local structure of turbulence in incompressible viscous fluid for very large Reynolds numbers. *Doklady Akademii Nauk SSSR*, *30*, 301–304.

Kuhlbrodt, T., Jones, C., Sellar, A., Storkey, D., Blockley, E., Stringer, M., et al. (2018). The low-resolution version of HadGEM3 GC3.1: Development and evaluation for global climate. *Journal of Advances in Modeling Earth Systems*, *10*(11), 2865–2888. https://doi.org/10.1029/2018ms001370

Kuhlbrodt, T., Smith, R. S., Wang, Z., & Gregory, J. M. (2012). The influence of eddy parameterizations on the transport of the Antarctic Circumpolar Current in coupled climate models. *Ocean Modelling*, *52–53*, 1–8. https://doi.org/10.1016/j.ocemod.2012.04.006

Lee, M.-M., & Coward, A. (2003). Eddy mass transport for the Southern Ocean in an eddy-permitting global ocean model. *Ocean Modelling*, *5*(3), 249–266. https://doi.org/10.1016/S1463-5003(02)00044-6

Leith, C. E. (1996). Stochastic models of chaotic systems. *Physica D: Nonlinear Phenomena*, *98*(2), 481–491. https://doi.org/10.1016/0167-2789(96)00107-8

Lumpkin, R., & Speer, K. (2007). Global Ocean meridional overturning. *Journal of Physical Oceanography*, *37*(10), 2550–2562. https://doi.org/10.1175/JPO3130.1

Madec, G., Bourdallé-Badie, R., Chanut, J., Clementi, E., Coward, A., Ethé, C., et al. (2019). NEMO ocean engine. In *Notes du Pôle de modélisation de l'Institut Pierre-Simon Laplace (IPSL)—Version 4.0* (p. 27). https://doi.org/10.5281/zenodo.3878122

Mak, J. (2023). Data collection for [FLAT_]UNAGI with splitting procedure. *Zenodo*. https://doi.org/10.5281/zenodo.8002828

Mak, J., Maddison, J. R., Marshall, D. P., & Munday, D. R. (2018). Implementation of a geometrically informed and energetically constrained mesoscale eddy parameterization in an Ocean Circulation model. *Journal of Physical Oceanography*, *48*(10), 2363–2382. https://doi.org/10.1175/JPO-D-18-0017.1

Mak, J., Marshall, D., Maddison, J. R., & Bachman, S. D. (2017). Emergent eddy saturation from an energy constrained eddy parameterisation. *Ocean Modelling*, *112*, 125–138. https://doi.org/10.1016/j.ocemod.2017.02.007

Mak, J., Marshall, D., Madec, G., & Maddison, J. R. (2022). Acute sensitivity of Global Ocean Circulation and heat content to eddy energy dissipation timescale. *Geophysical Research Letters*, *49*(8), e2021GL097259. https://doi.org/10.1029/2021GL097259

Marshall, D. (1995). Topographic steering of the Antarctic circumpolar current. *Journal of Physical Oceanography*, *25*(7), 1636–1650. https://doi.org/10.1175/1520-0485(1995)025⟨1636:TSOTAC⟩2.0.CO;2

Marshall, D., Maddison, J. R., & Berloff, P. S. (2012). A framework for parameterizing eddy potential vorticity fluxes. *Journal of Physical Oceanography*, *42*(4), 539–557. https://doi.org/10.1175/JPO-D-11-048.1

Marshall, J., Scott, J. R., Romanou, A., Kelley, M., & Leboissetier, A. (2017). The dependence of the Ocean's MOC on mesoscale eddy diffusivities: A model study. *Ocean Modelling*, *111*, 1–8. https://doi.org/10.1016/j.ocemod.2017.01.001

Marshall, J., & Speer, K. (2012). Closure of the meridional overturning circulation through Southern Ocean upwelling. *Nature Geoscience*, *5*(3), 171–180. https://doi.org/10.1038/ngeo1391

Megann, A. (2018). Estimating the numerical diapycnal mixing in an eddy-permitting ocean model. *Ocean Modelling*, *121*, 19–33. https://doi.org/10.1016/j.ocemod.2017.11.001

Megann, A., & Storkey, D. (2021). Exploring viscosity space in an eddy-permitting global ocean model: Is viscosity a useful control for numerical mixing? *Journal of Advances in Modeling Earth Systems*, *13*(5), e2020MS002263. https://doi.org/10.1029/2020MS002263

Megann, A., Storkey, D., Aksenov, Y., Alderson, S., Calvert, D., Graham, T., et al. (2014). GO5.0: The joint NERC–Met Office NEMO global ocean model for use in coupled and forced applications. *Geoscientific Model Development*, *7*(3), 1069–1092. https://doi.org/10.5194/gmd-7-1069-2014

Moreno-Chamarro, E., Caron, L.-P., Loosveldt Tomas, S., Vegas-Regidor, J., Gutjahr, O., Moine, M.-P., et al. (2022). Impact of increased resolution on long-standing biases in HighResMIP-PRIMAVERA climate models. *Geoscientific Model Development*, *15*(1), 269–289. https://doi.org/10.5194/gmd-15-269-2022

Munday, D. R., Johnson, H. L., & Marshall, D. (2015). The role of ocean gateways in the dynamics and sensitivity to wind stress of the early Antarctic Circumpolar Current. *Paleoceanography*, *30*(3), 284–302. https://doi.org/10.1002/2014PA002675

Pearson, B., Fox-Kemper, B., Bachman, S., & Bryan, F. (2017). Evaluation of scale-aware subgrid mesoscale eddy models in a global eddy-rich model. *Ocean Modelling*, *115*, 42–58. https://doi.org/10.1016/j.ocemod.2017.05.007

Petit, T., Robson, J., Ferreira, D., & Jackson, L. C. (2023). Understanding the sensitivity of the North Atlantic subpolar overturning in different resolution versions of HadGEM3-GC3.1. *Journal of Geophysical Research: Oceans*, *128*(10), e2023JC019672. https://doi.org/10.1029/2023JC019672

Petit, T., Robson, J., Ferreira, D., Yeager, S., & Evans, D. G. (2025). Coherence of the AMOC over the subpolar North Atlantic on interannual to multiannual time scales. *Geophysical Research Letters*, *52*(9), e2025GL115171. https://doi.org/10.1029/2025GL115171

Pezzi, L. P., de Souza, R. B., Santini, M. F., Miller, A. J., Carvalho, J. T., Parise, C. K., et al. (2021). Oceanic eddy-induced modifications to air–sea heat and CO_2 fluxes in the Brazil-Malvinas confluence. *Scientific Reports*, *11*(1), 10648. https://doi.org/10.1038/s41598-021-89985-9

Reynaud, T. H., Weaver, A. J., & Greatbatch, R. J. (1995). Summer mean circulation of the northwestern Atlantic Ocean. *Journal of Geophysical Research*, *100*(C1), 779–816. https://doi.org/10.1029/94JC02561

Rhein, M., Kieke, D., Hüttl-Kabus, S., Roessler, A., Mertens, C., Meissner, R., et al. (2011). Deep water formation, the subpolar gyre, and the meridional overturning circulation in the subpolar North Atlantic. *Deep Sea Research Part II: Topical Studies in Oceanography*, *58*(17–18), 1819–1832. https://doi.org/10.1016/j.dsr2.2010.10.061

Roberts, M. J., Baker, A., Blockley, E. W., Calvert, D., Coward, A., Hewitt, H. T., et al. (2019). Description of the resolution hierarchy of the global coupled HadGEM3-GC3.1 model as used in CMIP6 HighResMIP experiments. *Geoscientific Model Development*, *12*(12), 4999–5028. https://doi.org/10.5194/gmd-12-4999-2019

Sabine, C. L., Feely, R. A., Gruber, N., Key, R. M., Lee, K., Bullister, J. L., et al. (2004). The oceanic sink for anthropogenic CO_2. *Science*, *305*(5682), 367–371. https://doi.org/10.1126/science.1097403

Sallée, J.-B., Matear, R. J., Rintoul, S. R., & Lenton, A. (2012). Localized subduction of anthropogenic carbon dioxide in the Southern Hemisphere oceans. *Nature Geoscience*, *5*(8), 579–584. https://doi.org/10.1038/ngeo1523

Schubert, R., Gula, J., Greatbatch, R. J., Baschek, B., & Biastoch, A. (2020). The submesoscale kinetic energy cascade: Mesoscale absorption of submesoscale mixed layer eddies and frontal downscale fluxes. *Journal of Physical Oceanography*, *50*(9), 2573–2589. https://doi.org/10.1175/JPO-D-19-0311.1

Scott, R. B., & Wang, F. (2005). Direct evidence of an oceanic inverse kinetic energy cascade from satellite altimetry. *Journal of Physical Oceanography*, *35*(9), 1650–1666. https://doi.org/10.1175/JPO2771.1

19422466, 2025, 9, Downloaded from https://agupubs.onlinelibrary.wiley.com/doi/10.1029/2025MS004950 by NICE, National Institute for Health and Care Excellence, Wiley Online Library on [16/12/2025]. See the Terms and Conditions (https://onlinelibrary.wiley.com/terms-and-conditions) on Wiley Online Library for rules of use; OA articles are governed by the applicable Creative Commons License

Sellar, A. A., Jones, C. G., Mulcahy, J. P., Tang, Y., Yool, A., Wiltshire, A., et al. (2019). UKESM1: Description and evaluation of the U.K. Earth system model. *Journal of Advances in Modeling Earth Systems*, *11*(12), 4513–4558. https://doi.org/10.1029/2019MS001739

Sellar, A. A., Walton, J., Jones, C. G., Wood, R., Abraham, N. L., Andrejczuk, M., et al. (2020). Implementation of U.K. Earth system models for CMIP6. *Journal of Advances in Modeling Earth Systems*, *12*(4), e2019MS001946. https://doi.org/10.1029/2019MS001946

Shan, X., Sun, S., Wu, L., & Spall, M. (2024). Role of the Labrador current in the Atlantic meridional overturning circulation response to greenhouse warming. *Nature Communications*, *15*(1), 7361. https://doi.org/10.1038/s41467-024-51449-9

Smagorinsky, J. (1963). General circulation experiments with the primitive equations: I. The basic experiment. *Monthly Weather Review*, *91*(3), 99–164. https://doi.org/10.1175/1520-0493(1963)091⟨0099:GCEWTP⟩2.3.CO;2

Smith, R. S., Mathiot, P., Siahaan, A., Lee, V., Cornford, S. L., Gregory, J. M., et al. (2021). Coupling the U.K. Earth system model to dynamic models of the Greenland and Antarctic ice sheets. *Journal of Advances in Modeling Earth Systems*, *13*(10), e2021MS002520. https://doi.org/10.1029/2021MS002520

Soufflet, Y., Marchesiello, P., Lemarié, F., Jouanno, J., Capet, X., Debreu, L., & Benshila, R. (2016). On effective resolution in ocean models. *Ocean Modelling*, *98*, 36–50. https://doi.org/10.1016/j.ocemod.2015.12.004

Stewart, A. L., & Thompson, A. F. (2015). Eddy-mediated transport of warm circumpolar deep water across the Antarctic shelf Break. *Geophysical Research Letters*, *42*(2), 432–440. https://doi.org/10.1002/2014GL062281

Storkey, D., Blaker, A. T., Mathiot, P., Megann, A., Aksenov, Y., Blockley, E. W., et al. (2018). UK Global Ocean GO6 and GO7: A traceable hierarchy of model resolutions. *Geoscientific Model Development*, *11*(8), 3187–3213. https://doi.org/10.5194/gmd-11-3187-2018

Storkey, D., Mathiot, P., Bell, M. J., Copsey, D., Guiavarc'h, C., Hewitt, H. T., et al. (2025). Resolution dependence of interlinked Southern Ocean biases in global coupled HadGEM3 models. *Geoscientific Model Development*, *18*(9), 2725–2745. https://doi.org/10.5194/gmd-18-2725-2025

Tabeling, P. (2002). Two-dimensional turbulence: A physicist approach. *Physics Reports*, *362*(1), 1–62. https://doi.org/10.1016/S0370-1573(01)00064-3

Tagklis, F., Bracco, A., Ito, T., & Castelao, R. M. (2020). Submesoscale modulation of deep water formation in the Labrador Sea. *Scientific Reports*, *10*(1), 17489. https://doi.org/10.1038/s41598-020-74345-w

Tedesco, P., Gula, J., Penven, P., & Ménesguen, C. (2022). Mesoscale eddy kinetic energy budgets and transfers between vertical Modes in the Agulhas current. *Journal of Physical Oceanography*, *52*(4), 677–704. https://doi.org/10.1175/JPO-D-21-0110.1

Treguier, A. M., Held, I. M., & Larichev, V. D. (1997). Parameterization of Quasigeostrophic eddies in primitive equation ocean models. *Journal of Physical Oceanography*, *27*(4), 567–580. https://doi.org/10.1175/1520-0485(1997)027⟨0567:POQEIP⟩2.0.CO;2

Vallis, G. K. (2017). *Atmospheric and oceanic fluid dynamics: Fundamentals and large-scale circulation* (2nd ed.). Cambridge University Press. https://doi.org/10.1017/9781107588417

Vargas-Alemañy, J. A., Vigo, M. I., García-García, D., & Zid, F. (2023). Updated geostrophic circulation and volume transport from satellite data in the Southern Ocean. *Frontiers of Earth Science*, *11*, 1110138. https://doi.org/10.3389/feart.2023.1110138

Vernet, M., Geibert, W., Hoppema, M., Brown, P. J., Haas, C., Hellmer, H. H., et al. (2019). The Weddell Gyre, Southern Ocean: Present knowledge and future challenges. *Reviews of Geophysics*, *57*(3), 623–708. https://doi.org/10.1029/2018RG000604

Visbeck, M., Marshall, J., Haine, T., & Spall, M. (1997). Specification of eddy transfer coefficients in coarse-resolution ocean circulation models. *Journal of Physical Oceanography*, *27*(3), 381–402. https://doi.org/10.1175/1520-0485(1997)027⟨0381:SOETCI⟩2.0.CO;2

Voldoire, A., Saint-Martin, D., Sénési, S., Decharme, B., Alias, A., Chevallier, M., et al. (2019). Evaluation of CMIP6 DECK experiments with CNRM-CM6-1. *Journal of Advances in Modeling Earth Systems*, *11*(7), 2177–2213. https://doi.org/10.1029/2019MS001683

Wilder, T. (2025a). Code used to analyse data and produce figures for Wilder and Kuhlbrodt (2025)—Submitted to Journal of Advances in Modeling Earth systems (JAMES). [Software]. *Zenodo*. https://doi.org/10.5281/zenodo.15703784

Wilder, T. (2025b). NEMO source code to reproduce simulations in Wilder and Kuhlbrodt (2025)—Submitted to Journal of Advances in Modeling Earth Systems (JAMES). [Software]. *Zenodo*. https://doi.org/10.5281/zenodo.14620960

Wilder, T. (2025c). Supporting data to reproduce figures in Wilder and Kuhlbrodt (2025)—Submitted to Journal of Advances in Modeling Earth systems (JAMES). [Dataset]. *Zenodo*. https://doi.org/10.5281/zenodo.15703850

Williams, K., Copsey, D., Blockley, E. W., Bodas-Salcedo, A., Calvert, D., Comer, R., et al. (2018). The Met Office global coupled model 3.0 and 3.1 (GC3.0 and GC3.1) configurations. *Journal of Advances in Modeling Earth Systems*, *10*(2), 357–380. https://doi.org/10.1002/2017MS001115

Williams, R., Meijers, A. J. S., Roussenov, V. M., Katavouta, A., Ceppi, P., Rosser, J. P., & Salvi, P. (2024). Asymmetries in the Southern Ocean contribution to global heat and carbon uptake. *Nature Climate Change*, *14*(8), 823–831. https://doi.org/10.1038/s41558-024-02066-3

Worthington, E. L., Moat, B. I., Smeed, D. A., Mecking, J. V., Marsh, R., & McCarthy, G. D. (2021). A 30-year reconstruction of the Atlantic meridional overturning circulation shows no decline. *Ocean Science*, *17*(1), 285–299. https://doi.org/10.5194/os-17-285-2021

Worthington, E. L., Moat, B. I., Smeed, D. A., Mecking, J. V., Marsh, R., & McCarthy, G. D. (2022). AMOC reconstruction between 1981 and 2016 from hydrographic data using an empirical linear regression model from Worthington, E. L., Moat, B. I., Smeed, D. A., Mecking, J. V., Marsh, R., and McCarthy, G. D.: A 30-year reconstruction of the Atlantic meridional overturning circulation shows no decline, ocean Sci., 17, 285–299, doi: 10.5194/os-17-285-2021, 2021. *Zenodo* https://doi.org/10.5281/zenodo.6874313

Xavier, P., Willett, M., Graham, T., Earnshaw, P., Copsey, D., Narayan, N., et al. (2023). *Assessment of the met office global coupled model version 5 (GC5) configurations (report)*. Met Office/Met Office.

Yang, Z., Jing, Z., & Zhai, X. (2022). Effect of small-scale topography on eddy dissipation in the northern south China sea. *Journal of Physical Oceanography*, *52*(10), 2397–2416. https://doi.org/10.1175/JPO-D-21-0208.1

Youngs, M. K., Thompson, A. F., Lazar, A., & Richards, K. J. (2017). ACC Meanders, energy transfer, and mixed barotropic–baroclinic instability. *Journal of Physical Oceanography*, *47*(6), 1291–1305. https://doi.org/10.1175/JPO-D-16-0160.1

Zhai, X., & Greatbatch, R. J. (2006). Surface eddy diffusivity for heat in a model of the northwest Atlantic Ocean. *Geophysical Research Letters*, *33*(24), L24611. https://doi.org/10.1029/2006GL028712

Zhai, X., Johnson, H. L., & Marshall, D. (2010). Significant sink of ocean-eddy energy near western boundaries. *Nature Geoscience*, *3*(9), 608–612. https://doi.org/10.1038/ngeo943

Zhai, X., & Yang, Z. (2022). Eddy-induced meridional transport variability at ocean western boundary. *Ocean Modelling*, *171*, 101960. https://doi.org/10.1016/j.ocemod.2022.101960

19422466, 2025, 9, Downloaded from https://agupubs.onlinelibrary.wiley.com/doi/10.1029/2025MS004950 by NICE, National Institute for Health and Care Excellence, Wiley Online Library on [16/12/2025]. See the Terms and Conditions (https://onlinelibrary.wiley.com/terms-and-conditions) on Wiley Online Library for rules of use; OA articles are governed by the applicable Creative Commons License